



Universitat
de les Illes Balears

MASTER'S THESIS

TESTING WAVEFORM MODELS FOR THE LISA AND EINSTEIN TELESCOPE GRAVITATIONAL WAVE DETECTORS

Friso Snel

Master's Degree in Advanced Physics and Applied Mathematics

Centre for Postgraduate Studies

Academic Year 2019-20

TESTING WAVEFORM MODELS FOR THE LISA AND EINSTEIN TELESCOPE GRAVITATIONAL WAVE DETECTORS

Friso Snel

Master's Thesis

Centre for Postgraduate Studies

University of the Balearic Islands

Academic Year 2019-20

Key words:

LISA, Einstein Telescope, gravitational waves, waveform models

Thesis Supervisor's Name Dr. Sascha Husa

Abstract

The interest in gravitational waves has greatly increased since the first detection in 2015 [1]. This has given extra momentum to the development of new detectors, which will extend the accessible frequency range, while also improving the sensitivity compared to current detectors. Two of these detectors are studied here and they are the Einstein Telescope (ET) and the Laser Interferometer Space Antenna (LISA). The ET will probe the same frequency range as current detectors, though the band will be widened (to about 1 to 10^4 Hz) and the sensitivity will be much better. LISA will be an observatory in space and it will look for sources in an entirely new frequency range at about 10^{-4} to 1 Hz. A wide variety of sources is expected to be found by these detectors. Furthermore, they will have a much higher signal-to-noise ratio, which means that they can find out more information about the sources.

These new detectors will have sensitivity curves that are different from current detectors such as the Laser Interferometer Gravitational-Wave Observatory (LIGO), which means that their response to gravitational waves will be different. Some approximations were used for the LISA sensitivity curve and the consequence is that only the lower part of the LISA frequency range was considered in this work. A comparison was made between LISA, the ET and LIGO and it was found that LISA puts more emphasis on the merger, whereas the ET emphasizes the inspiral instead.

These different sensitivity curves could mean that the performance of waveform models is different. There are various methods for modelling gravitational waves from binary black holes. The three main families of waveform models that are used in parameter estimation (which means that they need to have a low computational cost) are compared. These are the phenomenological models IMRPhenomXHM [53] and IMRPhenomHM [52], the effective one-body reduced order model SEOBNRv4HM_ROM [54] and the hybrid surrogate model NRHybSur3dq8 [55]. All of these models use higher modes of the multipole expansion and are non-precessing.

The highest similarities were found between IMRPhenomXHM and NRHybSur3dq8. The overall performance for LIGO and the ET was similar, whereas the results for LISA were not as good. This depends on the choice of how to scale the mass between LIGO and LISA. The other results suggest that the matches for LISA might be better when the full response can be used to include higher frequencies. For both LISA and the ET it is found that the current models would induce systematic errors in parameter estimation.

Acknowledgments

First and foremost lots of thanks to my supervisor Dr. Sascha Husa, whose great help and support throughout this year made it possible to make this thesis. It has been quite an unusual way of working this year, but fortunately this situation was handled well through our many calls. Thanks to Dr. Alicia Sintes, Dr. Jaume Carrot and Dr. Sascha Husa for their great classes on gravitational waves and general relativity. I also want to thank Rodrigo Tenorio for helping me whenever I had questions for him and Alicia Calafat for our cooperation on various problems we have faced.

Contents

I	Introduction	4
1	General introduction	5
2	Introduction to Gravitational Waves	8
2.1	Linearized Gravity	8
2.2	Polarizations	13
2.3	Sources of gravitational waves	14
2.3.1	Binary star origin	16
2.3.2	Dynamical exchange	16
2.3.3	Supermassive black hole binaries	17
2.3.4	Other sources	18
3	Observation and data analysis	19
3.1	Antenna Pattern	21
3.2	Matched filtering	22
3.3	Parameter Estimation	23
3.3.1	Probability	24
3.3.2	Bayesian inference in gravitational wave astronomy	25
3.3.3	Markov chain Monte Carlo	27
3.4	Waveform models	27
3.4.1	Numerical Relativity	28
3.4.2	Alternative strategies	28
3.4.3	Higher modes	30
4	Einstein Telescope	32
4.1	Sources	32
4.1.1	Black hole binaries	33
4.1.2	Neutron stars	34
4.1.3	Tests of general relativity	35
4.1.4	New gravitational wave sources	35
4.2	Noise sources and sensitivity	35
4.2.1	Seismic noise and gravity gradient noise	36
4.2.2	Quantum noise	36
4.2.3	Thermal noise	37

5	LISA	38
5.1	Sources	39
5.1.1	Galactic binaries	40
5.1.2	Massive black holes	40
5.1.3	Extreme mass ratio inspirals	42
5.1.4	Stellar Origin Black Holes	43
5.1.5	Nature of gravity and black holes	43
5.1.6	Measure the rate of expansion of the Universe	44
5.1.7	Stochastic gravitational wave background	44
5.1.8	Gravitational wave bursts and unforeseen sources	44
5.2	Time Delay Interferometry	44
5.3	LISA response	46
II	Results	49
6	Comparison of inspiral, merger and ringdown sensitivities	50
6.1	Whitening	50
6.2	Inspiral, merger and ringdown	51
6.3	Results	52
7	Model comparison	64
7.1	Monte Carlo simulation	66
7.2	Results	66
8	Conclusions	71
	Bibliography	73

Part I

Introduction

Chapter 1

General introduction

The theory of general relativity, published by Albert Einstein in 1915, uses geometry to describe gravity. In general relativity the relationship between matter and the geometry of spacetime is described by the Einstein field equations:

$$G_{\mu\nu} = \frac{8\pi G}{c^4} T_{\mu\nu}. \quad (1.1)$$

The $G_{\mu\nu}$ on the left-hand side of this equation is the Einstein tensor that describes the curvature of spacetime, whereas the $T_{\mu\nu}$ on the right-hand side describes the distribution of matter. Matter bends the spacetime according to equation 1.1. Free particles, i.e. free from all non-gravitational forces, will move along paths called *geodesics*. These are the straightest possible lines through this curved space. The curvature of these paths is what is perceived as gravity.

A year after publishing the theory of general relativity Einstein made the prediction that accelerated masses can create ripples in the fabric of spacetime that can travel as waves at the speed of light. This is what we know as gravitational waves. Almost a hundred years later the first direct detection of a gravitational wave [1] was made by the instruments at the Hanford and Livingston sites (in the United States) of the Laser Interferometer Gravitational-Wave Observatory (LIGO). Both of these sites have interferometers with 4 km long arms separated by a 90° angle. The waves created by the merger of a binary black hole caused very small changes in the arm lengths of these detectors on the 14th of September 2015. These changes were detected and it was concluded that they were caused by a gravitational wave. The event was named GW150914 after the date of its detection.

GW150914 ushered in a new era of astronomy. Until then almost all astronomical information came from electromagnetic radiation, so an entirely new window for observing the Universe had been opened. Astronomy using electromagnetic radiation began by only using the visible part of the electromagnetic spectrum. Later on other parts of the spectrum were added, such as X-ray or radio wavelengths. Very different types of sources can be observed in different parts of the electromagnetic spectrum.

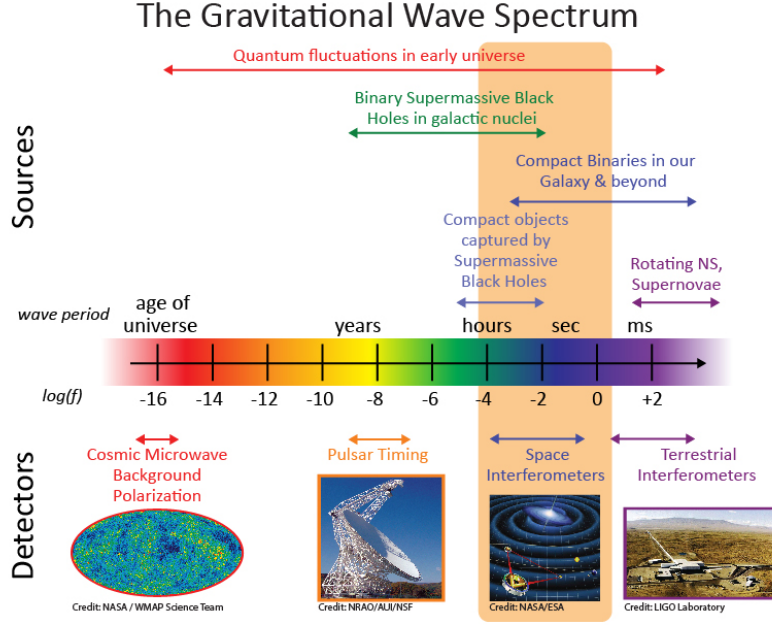


Figure 1.1: Gravitational wave spectrum, showing sources and detectors for different frequencies. Source: [3].

Similar things can be expected for gravitational wave astronomy.

Current ground-based gravitational wave detectors operate in the frequency range of about $10^1 - 10^3$ Hz, but many interesting sources are found in lower frequency ranges. Figure 1.1 gives an overview of several types of sources and detectors along the gravitational wave spectrum. The frequency range below that of ground-based detectors can be probed using space-based detectors. There are several several proposals for space-based detectors, of which the Laser Interferometer Space Antenna (LISA) is in an advanced stage; scheduled to be launched in 2034.

LISA will consist of three spacecraft in an equilateral triangle with sides of 2.5 million km. LISA will cover the frequency range of below 10^{-4} Hz till about 1 Hz [2]. Many interesting sources are expected to be found in this range and these are described in section 5.1.

Besides this new frequency window that will be opened by LISA there are also plans to improve the observations at frequencies accessible to current ground-based detectors. This can be achieved by building bigger detectors and one proposal to do this is the Einstein Telescope (ET). The ET has a triangular shape (contrary to the L-shapes in current usage) and has 10 km arms. It will have much better sensitivity at all frequencies and the frequency range it can cover is also bigger than those of current detectors.

For analysing the data of LISA and the ET (or gravitational wave detectors in general) theoretical waveform models play an important role. First the detector data is compared to waveforms in a template bank. This is a collection of many (a few 100.000 in the case of LIGO) waveforms with varying parameters (e.g. component

masses and spins in a binary coalescence). A good match between a template waveform and the data is an indication of a gravitational wave detection with parameters similar to those of the template. Once this happens the parameter space around the values of the template is explored stochastically to see which parameter values best fit the signal. In this process a large number of waveforms are produced and compared to the signal. A Bayesian posterior probability distribution is then produced for the parameters. Because one needs to produce a large amount (typically more than 10^7) of waveforms one will need an efficient method of producing these. Here we consider waveform models for binary black holes. There are several techniques for producing these, which are described in section 3.4. For LISA the requirements on these techniques are different than for ground-based detectors like LIGO, mostly because of the much higher signal-to-noise ratios (SNR) that are expected for LISA, which leads to higher requirements on the accuracy of the waveforms. In this work it is tested how well current techniques of efficiently producing waveforms work for LISA and the ET.

First a general introduction to gravitational waves is given in chapter 2. It discusses how the wave equation is derived, along with the two polarizations. Then it describes what kind of sources can produce gravitational waves that we could detect. Chapter 3 explains the principles of gravitational wave detectors and how their data is analyzed. The introduction is concluded with the chapters 4 and 5, which describe the LISA and ET gravitational wave detectors.

The results will consist of an analysis of how LIGO, LISA and the ET respond to different phases of gravitational waves, which are commonly divided into three phases (inspiral, merger and ringdown) as described in section 6.2. Chapter 6 describes these results. Finally a comparison is made of how the three main families of waveform models perform for each of the detectors. These results are given in chapter 7, after which the conclusions are summarized in chapter 8.

Introduction to Gravitational Waves

The Einstein field equations (equation 1.1) constitute a set of 16 coupled, non-linear differential equations (of which only 10 are independent, because of symmetry). Finding analytical solutions is very difficult and only few exist. The trivial solution is the one for flat space. This solution is the Minkowski metric, denoted here as $\eta_{\mu\nu}$. The Minkowski metric is the solution of special relativity, where there is no gravitational field, and, in matrix-form and Cartesian initial coordinates, it is equal to

$$\eta_{\mu\nu} = \begin{pmatrix} -1 & 0 & 0 & 0 \\ 0 & 1 & 0 & 0 \\ 0 & 0 & 1 & 0 \\ 0 & 0 & 0 & 1 \end{pmatrix}. \quad (2.1)$$

In this case there is no curvature and because of that it is commonly called flat space. A gravitational wave can be described as a perturbation on this flat space.

2.1 Linearized Gravity

Linearized gravity can be used to greatly simplify the Einstein field equations in the case of a weak gravitational field. In this case space will be close to flat and thus the metric $g_{\mu\nu}$ can be written as the Minkowski metric with a small perturbation $h_{\mu\nu}$:

$$g_{\mu\nu} = \eta_{\mu\nu} + h_{\mu\nu}, \quad |h_{\mu\nu}| \ll 1. \quad (2.2)$$

To linearize the Einstein field equations, equation 2.2 is plugged in and all terms that are not linear in $g_{\mu\nu}$ are dropped. First the Christoffel symbols are linearized, which are defined as

$$\Gamma_{\beta\gamma}^{\alpha} = \frac{1}{2}g^{\alpha\mu}(\partial_{\gamma}g_{\mu\beta} + \partial_{\beta}g_{\mu\gamma} - \partial_{\mu}g_{\gamma\beta}).$$

Plugging in equation 2.2 then gives:

$$\Gamma_{\beta\gamma}^{\alpha} = \frac{1}{2}(\eta^{\alpha\mu} + h^{\alpha\mu})(\partial_{\gamma}(\eta_{\mu\beta} + h_{\mu\beta}) + \partial_{\beta}(\eta_{\mu\gamma} + h_{\mu\gamma}) - \partial_{\mu}(\eta_{\gamma\beta} + h_{\gamma\beta})).$$

Now, noting that the derivatives of the flat metric vanish and omitting the terms that are quadratic in h (so removing the h in first parentheses and the η s in the second parentheses), we get

$$\Gamma_{\beta\gamma}^{\alpha} = \frac{1}{2}\eta^{\alpha\mu}(\partial_{\gamma}h_{\mu\beta} + \partial_{\beta}h_{\mu\gamma} - \partial_{\mu}h_{\gamma\beta}).$$

This can now be used to linearize the Riemann tensor, defined as

$$R_{\beta\gamma\delta}^{\alpha} = \partial_{\gamma}\Gamma_{\delta\beta}^{\alpha} - \partial_{\delta}\Gamma_{\gamma\beta}^{\alpha} + \Gamma_{\gamma\mu}^{\alpha}\Gamma_{\delta\beta}^{\mu} - \Gamma_{\delta\mu}^{\alpha}\Gamma_{\gamma\beta}^{\mu}.$$

The last two terms can be dropped immediately, because the Christoffel symbols are linear in h , so these terms are quadratic. This results in

$$\begin{aligned} R_{\beta\gamma\delta}^{\alpha} &= \partial_{\gamma}\frac{1}{2}\eta^{\alpha\mu}(\partial_{\beta}h_{\mu\delta} + \partial_{\delta}h_{\mu\beta} - \partial_{\mu}h_{\beta\delta}) - \partial_{\delta}\frac{1}{2}\eta^{\alpha\mu}(\partial_{\beta}h_{\mu\gamma} + \partial_{\gamma}h_{\mu\beta} - \partial_{\mu}h_{\beta\gamma}), \\ R_{\beta\gamma\delta}^{\alpha} &= \frac{1}{2}\eta^{\alpha\mu}(\partial_{\gamma}\partial_{\beta}h_{\mu\delta} - \partial_{\delta}\partial_{\beta}h_{\mu\gamma} - \partial_{\gamma}\partial_{\mu}h_{\beta\delta} + \partial_{\delta}\partial_{\mu}h_{\beta\gamma}). \end{aligned}$$

To get $R_{\alpha\beta\gamma\delta}$ we simply lower the index with $\eta_{\mu\alpha}$, which just removes the $\eta^{\mu\alpha}$ in $R_{\beta\gamma\delta}^{\alpha}$, so (immediately renaming μ back to α):

$$R_{\alpha\beta\gamma\delta} = \frac{1}{2}(\partial_{\gamma}\partial_{\beta}h_{\alpha\delta} - \partial_{\delta}\partial_{\beta}h_{\alpha\gamma} - \partial_{\gamma}\partial_{\alpha}h_{\beta\delta} + \partial_{\delta}\partial_{\alpha}h_{\beta\gamma}).$$

To obtain the Ricci tensor $R_{\beta\delta}$, the Riemann tensor has to be contracted as such: $R_{\beta\delta} = \eta^{\alpha\gamma}R_{\alpha\beta\gamma\delta}$. In the first term we raise the α , in the others the γ :

$$\eta^{\alpha\gamma}R_{\alpha\beta\gamma\delta} = \frac{1}{2}(\partial_{\gamma}\partial_{\beta}h_{\delta}^{\gamma} - \partial_{\delta}\partial_{\beta}h_{\alpha}^{\alpha} - \partial^{\alpha}\partial_{\alpha}h_{\beta\delta} + \partial_{\delta}\partial_{\alpha}h_{\beta}^{\alpha}).$$

Renaming the indices α and γ to μ , renaming β to α and δ to β and writing $h = h_{\mu}^{\mu}$ and $\square \equiv \partial^{\mu}\partial_{\mu}$ we have

$$R_{\alpha\beta} = \frac{1}{2}(\partial_{\mu}\partial_{\alpha}h_{\beta}^{\mu} - \partial_{\beta}\partial_{\alpha}h - \square h_{\alpha\beta} + \partial_{\beta}\partial_{\mu}h_{\alpha}^{\mu}).$$

Then, to get the Ricci scalar, this is contracted with $\eta^{\alpha\beta}$:

$$R = \eta^{\alpha\beta}R_{\alpha\beta} = \frac{1}{2}(\partial_{\mu}\partial_{\alpha}h^{\mu\alpha} - \partial^{\alpha}\partial_{\alpha}h - \square h_{\alpha}^{\alpha} + \partial_{\beta}\partial_{\mu}h^{\mu\beta}),$$

where the β is raised in the first three terms and the α in the last. Renaming μ to β in first term and μ to α in the last, we get

$$R = \partial_{\alpha}\partial_{\beta}h^{\alpha\beta} - \square h.$$

The Einstein tensor $G_{\alpha\beta}$ is defined as

$$G_{\alpha\beta} = R_{\alpha\beta} - \frac{1}{2}g_{\alpha\beta}R.$$

Combining all this, the Einstein field equations (equation 1.1) can be written as

$$\partial_\mu \partial_\alpha h_\beta^\mu - \partial_\beta \partial_\alpha h - \square h_{\alpha\beta} + \partial_\beta \partial_\mu h_\alpha^\mu - \eta_{\alpha\beta}(\partial_\mu \partial_\nu h^{\mu\nu} - \square h) = \frac{16\pi}{c^4} T_{\alpha\beta},$$

which can be simplified by using the trace reversed of $h_{\mu\nu}$, denoted $\bar{h}_{\mu\nu}$:

$$\bar{h}_{\mu\nu} = h_{\mu\nu} - \frac{1}{2}\eta_{\mu\nu}h. \quad (2.3)$$

Then the Einstein field equations can be written as

$$\square \bar{h}_{\mu\nu} + \eta_{\mu\nu} \partial^\rho \partial^\sigma \bar{h}_{\rho\sigma} - \partial^\rho \partial_\nu \bar{h}_{\mu\rho} - \partial^\rho \partial_\mu \bar{h}_{\nu\rho} = -\frac{16\pi}{c^4} T_{\mu\nu}. \quad (2.4)$$

This equation can be simplified using gauge freedom. Considering a small coordinate transformation

$$x'^\mu = x^\mu + \xi^\mu(x),$$

where $\xi^\mu(x)$ varies slowly, i.e. $|\partial_\alpha \xi_\beta| \ll 1$, the transformation between x' and x is (to first order)

$$\frac{\partial x^\mu}{\partial x'^\alpha} = \delta_\alpha^\mu - \frac{\partial \xi^\alpha}{\partial x^\mu}.$$

Plugging this into

$$g'_{\alpha\beta} = \frac{\partial x^\mu}{\partial x'^\alpha} \frac{\partial x^\nu}{\partial x'^\beta} g_{\mu\nu}$$

yields:

$$\eta_{\alpha\beta} + h'_{\alpha\beta} = (\delta_\alpha^\mu - \partial_\alpha \xi^\mu)(\delta_\beta^\nu - \partial_\beta \xi^\nu)(\eta_{\mu\nu} + h_{\mu\nu}).$$

From this equation we only keep the terms up to first order (so only terms containing one or less factors of $\{h_{\mu\nu}, \partial_\alpha \xi^\mu, \partial_\beta \xi^\nu\}$). This yields

$$\eta_{\alpha\beta} + h'_{\alpha\beta} = -\delta_\alpha^\mu \partial_\beta \xi^\nu \eta_{\mu\nu} - \partial_\alpha \xi^\mu \delta_\beta^\nu \eta_{\mu\nu} + \delta_\alpha^\mu \delta_\beta^\nu \eta_{\mu\nu} + \delta_\alpha^\mu \delta_\beta^\nu h_{\mu\nu}.$$

This is easily simplified to

$$h'_{\alpha\beta} = h_{\alpha\beta} - \partial_\alpha \xi_\beta - \partial_\beta \xi_\alpha. \quad (2.5)$$

Since $|\partial_\alpha \xi_\beta| \ll 1$ this new $h'_{\alpha\beta}$ again satisfies equation 2.2, we know that h and h' describe the same system when they are related as in equation 2.5. Thus we try to choose h' in such a way that it simplifies equation 2.4. Clearly equation 2.4 would be greatly simplified if

$$\partial^\nu \bar{h}_{\mu\nu} = 0. \quad (2.6)$$

Fortunately it turns out that this can be achieved by choosing the right gauge. Let's first get an expression for $\bar{h}_{\mu\nu}$. Equations 2.3 and 2.5 can be combined to write

$$\begin{aligned}
\bar{h}'_{\mu\nu} &= h_{\mu\nu} - \partial_\mu \xi_\nu - \partial_\nu \xi_\mu - \frac{1}{2} \eta_{\mu\nu} \eta^{\alpha\beta} (h_{\alpha\beta} - \partial_\alpha \xi_\beta - \partial_\beta \xi_\alpha) \\
&= \bar{h}_{\mu\nu} - \partial_\mu \xi_\nu - \partial_\nu \xi_\mu - \frac{1}{2} \eta_{\mu\nu} \eta^{\alpha\beta} (\partial_\alpha \xi_\beta - \partial_\beta \xi_\alpha) \\
&= \bar{h}_{\mu\nu} - \partial_\mu \xi_\nu - \partial_\nu \xi_\mu - \frac{1}{2} \eta_{\mu\nu} (-\partial^\beta \xi_\beta - \partial^\alpha \xi_\alpha) \\
&= \bar{h}_{\mu\nu} - \partial_\mu \xi_\nu - \partial_\nu \xi_\mu + \eta_{\mu\nu} \partial^\beta \xi_\beta.
\end{aligned}$$

Then $\partial^\nu \bar{h}_{\mu\nu}$ can be expressed as:

$$\begin{aligned}
\partial^\nu \bar{h}_{\mu\nu} &= \partial^\nu \bar{h}_{\mu\nu} - \partial^\nu \partial_\mu \xi_\nu - \partial^\nu \partial_\nu \xi_\mu + \partial^\nu \eta_{\mu\nu} \partial^\beta \xi_\beta \\
&= \partial^\nu \bar{h}_{\mu\nu} - \partial^\nu \partial_\mu \xi_\nu - \partial^\nu \partial_\nu \xi_\mu + \partial_\mu \partial^\beta \xi_\beta \\
&= \partial^\nu \bar{h}_{\mu\nu} - \partial^\nu \partial_\nu \xi_\mu + \partial_\mu \partial^\beta \xi_\beta - \partial_\mu \partial^\nu \xi_\nu \\
&= \partial^\nu \bar{h}_{\mu\nu} - \partial^\nu \partial_\nu \xi_\mu.
\end{aligned}$$

So to get $\partial^\nu \bar{h}_{\mu\nu} = 0$ it is required that $\square \xi_\mu = \partial^\nu \bar{h}_{\mu\nu}$, where $\square \equiv \partial^\nu \partial_\nu$. The equation $\square f = g$ always has a solution for well behaved g , so we can always choose coordinates in which $\partial^\nu \bar{h}_{\mu\nu} = 0$. Plugging this into equation 2.4 simply leaves

$$\square \bar{h}_{\mu\nu} = -\frac{16\pi}{c^4} T_{\mu\nu}. \quad (2.7)$$

To study the propagation of gravitational waves we shall look at this equation in the absence of matter, i.e. where $T_{\mu\nu} = 0$, so equation 2.7 simply becomes

$$\square \bar{h}_{\mu\nu} = 0. \quad (2.8)$$

Since $\square = -(1/c^2) \partial^2 / \partial t^2 + \nabla^2$, this is the equation of a wave traveling at speed c :

$$\frac{\partial^2 \bar{h}(t, x)}{\partial t^2} = -c^2 \nabla^2 \bar{h}(t, x).$$

A set of solutions to this equation is

$$\bar{h}_{\mu\nu} = A_{\mu\nu} \exp(ik_\nu x^\nu). \quad (2.9)$$

Plugging this into equation 2.8 gives

$$k_\alpha k^\alpha = 0.$$

When k is written as $k = (\omega, k^1, k^2, k^3)$ this means that $\omega^2 = (k^1)^2 + (k^2)^2 + (k^3)^2$. Using the Lorentz gauge condition means that:

$$\partial^\nu \bar{h}_{\mu\nu} = 0 \quad \rightarrow \quad A_{\mu\nu} k^\nu = 0. \quad (2.10)$$

These impose four conditions on $A_{\mu\nu}$ and so its 10 independent components have been reduced to 6. Now after imposing the Lorentz condition there is still some freedom left in the choice of coordinates. A further coordinate change

$$x'^\mu = x^\mu + \xi^\mu(x)$$

will still satisfy the gauge condition if $\square\xi_\mu = 0$. We can choose a similar set of solutions for this:

$$\xi_\mu = B_\mu \exp(ik_\sigma x^\sigma), \quad (2.11)$$

using

$$\bar{h}'_{\mu\nu} = \bar{h}_{\mu\nu} - \partial_\mu \xi_\nu - \partial_\nu \xi_\mu + \eta_{\mu\nu} \partial^\beta \xi_\beta \quad (2.12)$$

again. Using equation 2.12, 2.9 and 2.11 and dividing by the exponent gives

$$A'_{\mu\nu} = A_{\mu\nu} - ik_\mu B_\nu - ik_\nu B_\mu + i\eta_{\mu\nu} B^\beta k_\beta. \quad (2.13)$$

Now we want to impose what is called the transverse-traceless (TT) gauge, in which

$$A_{0\nu} = 0 \quad (\text{transverse}), \quad (2.14)$$

$$A^\mu_\mu = 0 \quad (\text{traceless}). \quad (2.15)$$

To get condition 2.15, first 2.13 is contracted with $\eta^{\mu\nu}$ to get

$$A'^\mu_\mu = A^\mu_\mu - ik_\mu B^\mu - ik^\mu B_\mu + i\eta^\mu_\mu B^\beta k_\beta. \quad (2.16)$$

Now $k^\mu B_\mu = \eta^{\alpha\mu} k_\alpha B_\mu = k_\alpha B^\alpha$ and $\eta^\mu_\mu = 4$, so combining 2.16 and 2.15 gives

$$A'^\mu_\mu = 0 = A^\mu_\mu + 2iB^\beta k_\beta \quad \rightarrow \quad B^\beta k_\beta = \frac{i}{2}A^\mu_\mu. \quad (2.17)$$

Now first condition 2.14 is solved for $\nu = 0$, using 2.17:

$$\begin{aligned} A'_{00} = 0 &= A_{00} - ik_0 B_0 + i\eta_{00} B^\beta k_\beta \\ 0 &= A_{00} - 2ik_0 B_0 + \frac{1}{2}A^\mu_\mu \\ B_0 &= -\frac{i}{2k_0}(A_{00} + \frac{1}{2}A^\mu_\mu). \end{aligned}$$

Next B_j is solved for $j = 1, 2, 3$ (using $\eta_{0j} = 0$):

$$\begin{aligned} 0 &= A_{0j} - ik_0 B_j - ik_j B_0 + \eta_{0j} B^\beta k_\beta \\ &= A_{0j} - ik_0 B_j - ik_j \left(-\frac{i}{2k_0}(A_{00} + \frac{1}{2}A^\mu_\mu)\right) \\ B_j &= -\frac{iA_{0j}}{k_0} + \frac{i}{2k_0^2}(A_{00} + \frac{1}{2}A^\mu_\mu). \end{aligned}$$

So by choosing B like this the conditions 2.15 and 2.14 are satisfied. We can now choose the wave vector k^μ so that it's traveling in the z -direction, meaning: $k = (\omega, 0, 0, \omega)$. We know that $A_{\mu\nu}k^\mu = 0$ (equation 2.10), so

$$A_{0\nu}k^0 + A_{1\nu}k^1 + A_{2\nu}k^2 + A_{3\nu}k^3.$$

We also know that $A_{0\nu} = 0$ (equation 2.6), $k_1 = k_2 = 0$ and $k^3 \neq 0$, so therefore $A_{3\nu} = 0$. Since A is also traceless (equation 2.15) and symmetric this means that

$$A = \begin{pmatrix} 0 & 0 & 0 & 0 \\ 0 & A_+ & A_\times & 0 \\ 0 & A_\times & -A_+ & 0 \\ 0 & 0 & 0 & 0 \end{pmatrix}.$$

Plugging this into equation 2.9, taking the real part and noting that $\bar{h}_{\mu\nu} = h_{\mu\nu}$ when traceless gives

$$h_{\mu\nu} = \begin{pmatrix} 0 & 0 & 0 & 0 \\ 0 & h_+ & h_\times & 0 \\ 0 & h_\times & -h_+ & 0 \\ 0 & 0 & 0 & 0 \end{pmatrix} \cos(\omega(t - \frac{z}{c})),$$

with h_+ and h_\times constants.

2.2 Polarizations

To see how a gravitational wave will affect test particles we shall use the geodesic deviation equation:

$$\frac{d^2}{d\tau^2}S^\mu = R^\mu_{\nu\rho\sigma}U^\nu U^\rho S^\sigma.$$

This is used to describe the relative motion of nearby particles. S^μ is the separation between the particles, R the Riemann tensor and U the four-velocity of the particles. For slowly moving particles U will be equal to $(1,0,0,0)$ plus corrections of the order of $h_{\mu\nu}$. Since the Riemann tensor already is of order $h_{\mu\nu}$ these corrections will be of higher order and will be ignored. So taking $U = (1,0,0,0)$ we only need to consider $\nu = \rho = 0$. Then the linearized Riemann tensor will be

$$R_{\mu 00\sigma} = \frac{1}{2}(\partial_0\partial_0 h_{\mu\sigma} + \partial_\sigma\partial_\mu h_{00} - \partial_\sigma\partial_0 h_{\mu 0} - \partial_\mu\partial_0 h_{\sigma 0}),$$

but $h_{\mu 0} = h_{0\mu} = 0$ so only the first term is left. Also, for slowly moving particles $t = \tau$ to lowest order, so we are left with

$$\frac{\partial^2}{\partial t^2}S^\mu = \frac{1}{2}S^\sigma \frac{\partial^2}{\partial t^2}h_{\mu\sigma}. \quad (2.18)$$

Taking the xy-plane and a gravitational wave traveling in the z-direction:

$$h = \begin{pmatrix} 0 & 0 & 0 & 0 \\ 0 & h_+ & h_\times & 0 \\ 0 & h_\times & -h_+ & 0 \\ 0 & 0 & 0 & 0 \end{pmatrix} \sin(\omega t). \quad (2.19)$$

Now we first take $h_\times = 0$. The separation should be an equilibrium position plus a perturbation from this equilibrium: $S = (x_0 + \delta x(t), y_0 + \delta y(t))$. Using 2.18 and 2.19 this gives the equations

$$\begin{aligned} \frac{\partial^2}{\partial t^2} \delta x(t) &= -\frac{\omega^2}{2} h_+ (x_0 + \delta x(t)) \sin(\omega t), \\ \frac{\partial^2}{\partial t^2} \delta y(t) &= \frac{\omega^2}{2} h_+ (y_0 + \delta y(t)) \sin(\omega t), \end{aligned}$$

which can be solved to give

$$\delta x(t) = \frac{h_+}{2} x_0 \sin(\omega t), \quad (2.20)$$

$$\delta y(t) = -\frac{h_+}{2} y_0 \sin(\omega t). \quad (2.21)$$

In an analogous manner the expressions for the h_\times component are found to be

$$\delta x(t) = \frac{h_\times}{2} y_0 \sin(\omega t), \quad (2.22)$$

$$\delta y(t) = \frac{h_\times}{2} x_0 \sin(\omega t). \quad (2.23)$$

2.3 Sources of gravitational waves

Gravitational radiation has similarities to electromagnetic radiation. Electromagnetic waves are emitted by accelerating charges, whereas gravitational radiation comes from accelerating masses. Both types of radiation travel at the speed of light and there might be a particle associated with both of them (the photon with electromagnetic radiation and the hypothetical graviton for gravitational radiation). An important distinction is that gravity is always attractive (there is only one type of “charge”), whereas electromagnetic forces can be attractive or repulsive (there are two types of charge).

One can express the radiation in a multipole expansion and conclude that the first term will come from the quadrupole in the case of gravitational waves. The reasoning here follows [34]. When $\rho(\mathbf{r})$ represents the charge or mass-energy density then the monopole moment is equal to $\int \rho(\mathbf{r}) d\mathbf{r}^3$. This quantity does not vary because of the conservation of charge and mass-energy. Next is the “electric” dipole moment $\int \rho(\mathbf{r}) \mathbf{r} d\mathbf{r}^3$, which can vary and produce radiation in the electromagnetic case. For

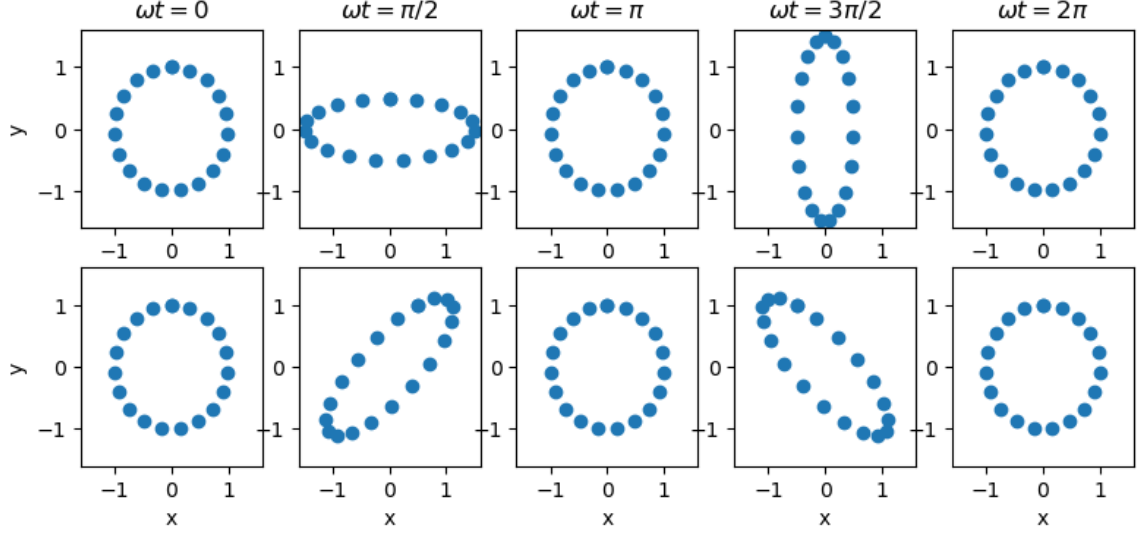


Figure 2.1: Positions of test masses for several values of ωt , using equations 2.20, 2.21, 2.22, 2.23. Top row: plus-polarized wave, bottom row: cross-polarized wave.

gravitational radiation this quantity is equal to the center of mass. This may vary in general, but it will be constant in the center of mass frame, so there won't be any radiation in that frame. Since the existence of radiation doesn't depend on the frame there won't be radiation in any frame. Then there is the “magnetic” dipole moment $\int \rho(\mathbf{r}) \mathbf{r} \times \mathbf{v}(\mathbf{r}) d\mathbf{r}^3$, which again may vary for the electromagnetic case. For the gravitational case this is just the angular momentum, a conserved quantity. One then arrives at the quadrupole $I_{ij} = \int \rho(\mathbf{r}) r_i r_j d\mathbf{r}^3$. Here there is no conservation law for the gravitational case so quadrupole radiation is permitted. This leading term in gravitational radiation was first derived by Albert Einstein in 1918 and reads

$$h_{ij}^{TT}(t, r) = \frac{2G}{c^4 r} \ddot{I}_{ij}(t - r/c), \quad (2.24)$$

where an overdot denotes differentiating with respect to time. The complete multipole expansion can be written as

$$h_+ - ih_\times = \sum_{l \geq 2} \sum_{m=-l}^l {}_{-2}Y_{lm}(\theta, \phi) h_{lm}, \quad (2.25)$$

where ${}_{-2}Y_{lm}(\theta, \phi)$ is the (l, m) mode of the -2 spin-weighted spherical harmonic for polar angle θ and azimuthal angle ϕ . The quadrupole term corresponds to the (2,2) and (2,-2) mode and it is the dominant term in the expansion. The significance of the higher modes depends on the parameters of the system, as described in section 3.4.3.

Any object with a varying mass quadrupole moment (or higher terms in the expansion) will emit gravitational waves. This means gravitational waves are created all the time all around us on Earth, it appears however that these are all far too faint to detect. In fact, the only sources that have caused detectable gravitational waves so far are some

of the most violent events in the Universe: mergers of black holes and/or neutron stars. These are large masses that are very compact and because of that they can orbit each other rapidly at a small separation, where energy loss through gravitational radiation will cause them merge eventually. Under all of these circumstances the system has a large and rapidly varying quadrupole moment, causing the emission of gravitational waves that can be strong enough to detect on Earth.

2.3.1 Binary star origin

There are several ways in which these binary black hole systems can be formed. Stellar black holes are formed in the gravitational collapse of a star and have a mass range of about $5 M_{\odot}$ up to several tens of M_{\odot} . The first way in which a binary stellar black hole could be formed is from a binary system of two high mass stars, as described in [35]. Gravitational radiation gets weak at large separations and, after the stars have collapsed, the black holes would have to be at a distance of a few solar radii in order to merge within a Hubble time. Massive stars can however get a size of up to a few thousands of solar radii near the end of their lifetime, so the separation will have to be larger initially. When one starts out with two massive main sequence stars at a sufficiently (so they won't merge prematurely when one turns into a giant) large separation, one of them will be the first to collapse and form a black hole. At some point after that the other will turn into a giant that will overflow its Roche lobe (where the outer layers will no longer be gravitationally bound to the star and mass transfer will occur) and this will lead to a common envelope of gas. The gas does not rotate at the same rate as the binary system constituents and thus the black hole and star core will be slowed down by drag, reducing their separation. This drag will transfer energy to the envelope, which might be ejected as a result of this energy. If the envelope is ejected the core can collapse to a black hole and the resulting black hole binary can merge (due to gravitational radiation) within a Hubble time. If the envelope is not ejected the two objects will merge prematurely and won't produce gravitational waves that can be (reasonably) measured. There is some uncertainty about the dynamics of these common envelopes and some alternative hypotheses have been proposed. A schematic overview of the process can be seen in figure 2.2.

2.3.2 Dynamical exchange

Another way in which binary black holes can be formed is through dynamical exchange [35], which can occur in dense regions. Star clusters are among the densest regions in the Universe and there are several types of them. Globular clusters [36] are found outside the thin disk of galaxies and orbit its center. Nuclear star clusters [37] are found near the center of most galaxies and open clusters [38] are the least massive but they are an important source of massive stars which could form a black hole [39].

The high density and low velocity dispersion in these regions mean that orbits in these regions are constantly being perturbed by dynamical encounters with other stars from the cluster. Encounters can occur between a binary star and a single star in which the single star replaces one of the constituents of the binary system; a process called dynamical exchange. Black holes are efficient in acquiring companions in this process [40, 41]. When a binary black hole is formed that is tightly bound has an

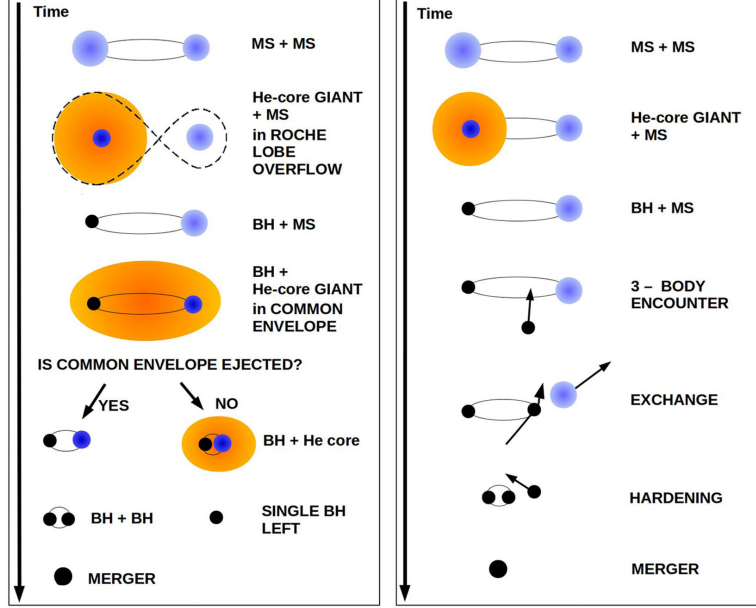


Figure 2.2: Binary black hole formation through massive binary system (left) and dynamical exchange, source: [35].

encounter with a third object it will exchange part of its internal energy with the third object. This can reduce the separation in the binary system which can bring them close enough to make energy loss through gravitational radiation efficient. Figure 2.2 gives a schematic view of this process.

2.3.3 Supermassive black hole binaries

Another potential source for measurable gravitational waves is a binary system of supermassive black holes. It is known that many galaxies have a supermassive black hole at their center and when galaxies merge these can form a binary system. When the galaxies merge the central supermassive black holes will move to central regions as a result of being slowed down by dynamical friction. At some point dynamical friction becomes inefficient, but interactions with surrounding stars and black holes can further decrease the separation. If these interactions can bring the system to a sufficiently small separation, energy loss due to the gravitational radiation can become significant, which lets the orbits decay further, finally leading to a merger.

Supermassive black hole binaries have been observed at a projected separation of about 7 pc [43] and a triple system has been observed with the smallest separation being about 140 pc [44]. For gravitational wave emission to get efficient enough to let the binary merge withing a Hubble time, the separation would have to decrease to roughly 0.01 pc. It is not exactly known how the separation can decrease this far. This problem has been called the “final parsec problem” [45] and several solutions have been proposed, e.g. [46, 47].

2.3.4 Other sources

So far all observed gravitational waves have come from merging neutron stars and/or black holes, but several other sources might be observed in the future. Examples are gravitational waves from supernova explosions or continuous waves from binary systems. These are discussed in sections 4.1 and 5.1.

Chapter 3

Observation and data analysis

The first attempt to build a gravitational wave detector came from Joseph Weber. He used an aluminum cylinder of a few meters that had a resonance frequency of about 1600 Hz. The idea was that a continuous gravitational wave signal at the right frequency would cause the cylinder to resonate, allowing the measurement of a varying length of the device. Weber first claimed to have detected gravitational waves in 1969 [60], but attempts to duplicate these results were unsuccessful. Through time some more Weber-type detectors have been constructed but none of these have ever been able to measure a gravitational wave.

Later on the focus shifted towards building L-shaped Michelson interferometers. These are often grouped into different generations. The so-called first generation was mostly for testing the technologies that would later be used by more sensitive detectors. It consists of the TAMA 300 with 300 m arms and CLIO with 100 m arms, which were both constructed in Japan to do research for a future larger interferometer. Then there is the German GEO600 (600 m arms) and also the initial versions (with lower sensitivity, which was later upgraded) of LIGO (4 km arms) and Virgo (3 km arms).

The second generation started out with Advanced LIGO and Advanced Virgo, which to date are the only observatories that have been used in a detection. These detectors are very similar, with Virgo having a smaller arm length (at 3 km, compared to LIGO's 4 km). Figure 3.1 shows the LIGO site at Hanford. The Japanese KAGRA has recently been completed and has now joined them in the search for gravitational waves. This interferometer has 3 km arms and is the first to be constructed underground and to use cryogenic mirrors to reduce noise. In a few years this network will be further improved by the addition of LIGO India, with 4 km arms like the other LIGO sites.



Figure 3.1: LIGO site at Hanford, source: [27].

Figure 3.2 shows a schematic layout of an L-shaped interferometer. The laser is emitting light, of which half is directed into each arm by the beam splitter. There are two mirrors in the arm, one at the end and one near the beam splitter. The light bounces back and forth many times between these mirrors before being recombined at the beam splitter and continuing to the photodetector. The beam that is reflected by the beam splitter towards the photodetector gets a phase change of π , so the light will be exactly out of phase when the arm lengths are exactly equal. This means that there will be total destructive interference so the photodetector will not measure any power. When the arm lengths change there is no longer complete destructive interference and this will be measured by the photodetector.

The power measured at the photodetector is thus related to the strain (relative length change $\Delta L/L$, where L is the arm length). The sensitivity of the detector to gravitational waves depends on the direction and orientation of the source.

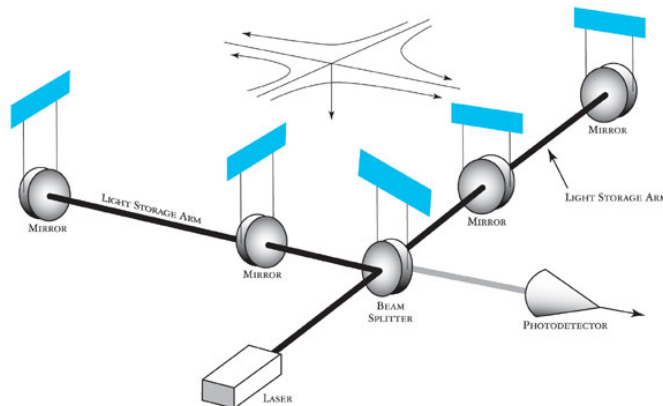


Figure 3.2: Schematic layout of L-shaped interferometer detector source: [28].

3.1 Antenna Pattern

Michelson interferometers measure the strain that is caused by a passing gravitational wave. From section 2.1 it is known what the metric perturbation of a gravitational wave looks like in a frame in which it is traveling along the z -axis and the plus polarization in the direction of the x -axis. We also know what effect a gravitational wave has on matter from section 2.2. By combining this an expression can be found for the signal from a gravitational wave coming at a detector from an arbitrary direction. The derivation here follows that of [23].

First we need to find a rotation matrix between the detector frame and the wave frame. For the detector we shall use an orthogonal reference frame in which the arms lie in the xy -plane and the angle between x and one arm is equal to the angle between y and the other arm. This angle shall be called ζ . We use a right-handed coordinate system such that the z -axis points up.

Now we imagine a gravitational wave (frame $\{x', y', z'\}$) coming in from an arbitrary direction \mathbf{n} towards the detector (frame $\{x, y, z\}$). So the positive z' axis will lie in the direction of $-\mathbf{n}$. The angle between \mathbf{n} and z shall be named θ , so the angle between z and z' is equal to $\pi - \theta$. Then we still need an angle to describe the direction of the x' axis. Let \mathbf{k} be a vector perpendicular to z' and lying in the $z'z$ -plane. This gives two possibilities and we shall take the one in the positive z direction. Then we name the angle between x' and \mathbf{k} ψ . Finally the angle between the projection of \mathbf{n} on the xy -plane and the x -axis shall be named ϕ .

The rotation matrix to take frame $\{x', y', z'\}$ into frame $\{x, y, z\}$ will be constructed with 3 Euler rotation matrices. First a rotation along the z -axis with an angle of $-\phi$, this will align the projection of \mathbf{n} on the xy -plane with the x -axis. Then a rotation along the y -axis of $\pi - \theta$. Now the z' -axis is aligned with the z -axis. Finally another rotation along the z -axis, now with an angle ψ will align all axes. The matrix will be:

$$M = R_z(-\phi)R_y(\pi - \theta)R_z(\psi),$$

$$M = \begin{pmatrix} \cos \phi & \sin \phi & 0 \\ -\sin \phi & \cos \phi & 0 \\ 0 & 0 & 1 \end{pmatrix} \begin{pmatrix} -\cos \theta & 0 & \sin \theta \\ 0 & 1 & 0 \\ -\sin \theta & 0 & \cos \theta \end{pmatrix} \begin{pmatrix} \cos \psi & \sin \psi & 0 \\ -\sin \psi & \cos \psi & 0 \\ 0 & 0 & 1 \end{pmatrix},$$

$$M = \begin{pmatrix} -\cos \phi \cos \theta \cos \psi + \sin \phi \sin \psi & \sin \phi \cos \psi + \cos \phi \cos \theta \sin \psi & \cos \phi \sin \theta \\ \sin \phi \cos \theta \cos \psi + \cos \phi \sin \psi & \cos \phi \cos \psi - \sin \phi \cos \theta \sin \psi & -\sin \phi \sin \theta \\ -\sin \theta \cos \psi & \sin \theta \sin \psi & -\cos \theta \end{pmatrix}. \quad (3.1)$$

Now the response of a gravitational wave detector in the long wavelength approximation is equal to

$$\frac{\Delta L(t)}{L} = \frac{1}{2} \hat{n}_1^T H \hat{n}_1 - \frac{1}{2} \hat{n}_2^T H \hat{n}_2. \quad (3.2)$$

where L is the length of the detector and $\hat{n}_{1,2}$ are the unit vectors pointing along the detectors arms. H is the gravitational wave tensor. Now the inverse of M is equal to

M^T , so for the gravitational wave tensor in the different frames we can write

$$H = MH'M^T. \quad (3.3)$$

The unit vectors can be written in the detector frame as:

$$\hat{n}_1 = \begin{bmatrix} \cos(\frac{\pi}{4} - \frac{\zeta}{2}) \\ \sin(\frac{\pi}{4} - \frac{\zeta}{2}) \\ 0 \end{bmatrix}, \quad \hat{n}_2 = \begin{bmatrix} \sin(\frac{\pi}{4} - \frac{\zeta}{2}) \\ \cos(\frac{\pi}{4} - \frac{\zeta}{2}) \\ 0 \end{bmatrix}. \quad (3.4)$$

Combining this leads to

$$\frac{\Delta L((t; \theta, \phi, \psi))}{L} = F_+(t; \theta, \phi, \psi)h_+ + F_\times(t; \theta, \phi, \psi)h_\times, \quad (3.5)$$

where $F_+(t; \theta, \phi, \psi)$ and $F_\times(t; \theta, \phi, \psi)$ are the detector pattern functions, given by

$$\begin{aligned} F_+(t; \theta, \phi, \psi) &= \sin \zeta [1/2(1 + \cos^2 \theta) \cos(2\phi) \cos(2\psi) - \cos \theta \sin(2\phi) \sin(2\psi)], \\ F_\times(t; \theta, \phi, \psi) &= -\sin \zeta [1/2(1 + \cos^2 \theta) \cos(2\phi) \cos(2\psi) - \cos \theta \sin(2\phi) \sin(2\psi)]. \end{aligned}$$

3.2 Matched filtering

The strain measured by a detector when a gravitational wave passes is a time series that can be written as

$$s(t) = n(t) + h(t), \quad (3.6)$$

where $s(t)$ is the measured signal, $n(t)$ is the noise and $h(t)$ is the signal from the gravitational wave. One will have to figure out if the measured signal contains a signal as in equation 3.6 or if it only consists of noise. The optimal technique of doing this, in the case of Gaussian stationary noise, is called *matched filtering*.

One will have to know the noise characteristics and a way to express this is through the Power Spectral Density. To define this we first introduce the Fourier transform convention used here. For a time series $x(t)$ the Fourier transform $\tilde{x}(f)$ is defined as

$$\tilde{x}(f) = \int_{-\infty}^{\infty} x(t) e^{-2i\pi f t} dt \quad (3.7)$$

and its inverse as

$$x(t) = \int_{-\infty}^{\infty} \tilde{x}(f) e^{2i\pi f t} df. \quad (3.8)$$

Now according to Parseval's theorem the total energy E of the signal is equal to

$$E = \int_{-\infty}^{\infty} |x(t)|^2 dt = \int_{-\infty}^{\infty} |\tilde{x}(f)|^2 df. \quad (3.9)$$

The quantity $|\tilde{x}(f)|^2$ gives the contribution to the total energy per unit frequency at the frequency f and is called the energy spectral density. This energy spectral density is only well-defined for a finite signal. Usually one will want to work with the power

spectral density S instead. This gives the contribution to the total power per unit frequency for a given frequency for a signal of infinite time T and can thus be written as

$$S(f) = \lim_{T \rightarrow \infty} \left| \int_{-T/2}^{T/2} x(t) e^{-2i\pi f t} dt \right|^2. \quad (3.10)$$

For a real signal (as is the case for the strain in gravitational wave astronomy) $\tilde{x}(f) = \tilde{x}(-f)^*$, where $*$ denotes complex conjugation, so $S(f) = S(-f)$ and all information is contained in the positive frequencies. This allows us to use the one-sided power spectral density (referred to as PSD hereafter), where only the positive values are used and they are multiplied by 2, so that the integral over all frequencies still gives the total power. The noise of a detector over a long period has a certain PSD, which shall be denoted as $S_n(f)$.

Using this the inner product $(a|b)$ between the signals a and b is defined as

$$(a|b) \equiv 2 \int_0^\infty \frac{\tilde{a}^*(f) \tilde{b}(f) + \tilde{a}(f) \tilde{b}^*(f)}{S_n(f)} df = 4 \int_0^\infty \frac{\tilde{a}^*(f) \tilde{b}(f)}{S_n(f)} df. \quad (3.11)$$

Similar to common definitions of the inner product between functions, but with the contributions weighted by the noise. Now the best SNR ρ that can be achieved for a signal h is

$$\rho^2 = (h|h) = 4 \int_0^\infty \frac{|\tilde{h}(f)|^2}{S_n(f)} df, \quad (3.12)$$

integrating the ratio between the signal PSD and noise PSD over all frequencies. In matched filter the signal of the detector is compared to a template waveform. A bank with a few 100.000 templates with different parameters is compared to the signal. When there is a certain threshold similarity between the template and the signal this could indicate the detection of a gravitational wave. The overlap \mathcal{O} is used to quantify the similarity between a signal h and a template $u(\theta)$, where θ is a parameter vector. The overlap is defined as

$$\mathcal{O}(\theta) = \frac{(h|u(\theta))}{\sqrt{(h|h)(u(\theta)|u(\theta))}}. \quad (3.13)$$

Its absolute value can be between 0 and 1, where 1 means h and u are equal (with the exception of multiplication by a constant). After finding a match, i.e. an overlap between template and signal above a certain threshold, the parameters of the template can be tuned to find what fits best in a procedure called parameter estimation.

3.3 Parameter Estimation

When there is a candidate gravitational wave event the parameters of its source are estimated through a method using Bayesian inference. Examples of these parameters

are the component masses and spins in the case of a binary coalescence. A probability distribution is computed which describes how likely certain parameter values are.

3.3.1 Probability

Probability describes the likelihood of some event to occur or how likely some statement is true. There are various interpretations on what probability would exactly mean and the most important of these are the frequentist and the Bayesian interpretation.

Frequentist

In the frequentist approach one can consider an experiment that can have various outcomes. The probability of each outcome is then the ratio at which this event occurs when repeating the experiment many times. When talking about hypotheses, e.g. if a certain political party will win an election, it wouldn't make sense for a frequentist to talk about a probability that this will occur, because the party will either win this particular election or it won't; this is not an experiment that can be repeated many times. Instead frequentists use *confidence intervals* to test hypotheses. A value that is often used is the 95% confidence interval, which means that one has a 95% confidence level (that is emphatically not a 95% probability) that the true value of the parameter is in this interval. What it means is that when a frequentist has computed many 95% confidence intervals for all kinds of different things, then 95% of these intervals will contain the true parameter value. The frequentist may accept or decline a hypothesis (that the parameter is equal to, or bigger/smaller than some value) with a certain significance, based on whether or not this value lies within a confidence interval of a certain size.

Bayesian

In the Bayesian approach probability is often described as the more subjective *degree of belief*. In the example of the political party one could have some information of polls and some personal ideas about the reliability of these polls and, in the Bayesian approach, one could use this to compute a probability of a certain party winning the election. The fundamental equation in Bayesian inference is Bayes' theorem. The general way to write this is

$$P(A|B) = \frac{P(B|A)P(A)}{P(B)}. \quad (3.14)$$

Where $P(A)$ is the probability of event A and $P(A|B)$ is the probability of event A given that event B has occurred. Some fundamental quantities in Bayesian inference are the posterior, likelihood, prior and evidence. If θ is a parameter vector and d the observed data then the prior $\pi(\theta)$ is a probability distribution that indicates some prior belief about the parameter values θ . This prior can be more or less subjective and can, for example, be based on previous research. The likelihood is the quantity $\mathcal{L}(d|\theta)$, so the interpretation of this is that it is the probability of getting the observed data given parameter values θ . Now the posterior distribution $p(\theta|d)$ (the probability distribution

of parameter values given the data) is the primary result of Bayesian inference and is given by

$$p(\theta|d) = \frac{\mathcal{L}(d|\theta)\pi(\theta)}{\mathcal{Z}}. \quad (3.15)$$

Now \mathcal{Z} is the normalization constant called the evidence and is thus given by

$$\mathcal{Z} \equiv \int \mathcal{L}(d|\theta)\pi(\theta)d\theta. \quad (3.16)$$

In Bayesian inference one talks about credible intervals instead of the frequentist's confidence intervals. A 95% credible interval $[A,B]$ means that there is a 95% *probability* (a frequentist wouldn't use this word for a parameter value) that the parameter value is in this interval. So

$$\int_A^B p(\theta|d)d\theta = 0.95. \quad (3.17)$$

3.3.2 Bayesian inference in gravitational wave astronomy

The description of Bayesian inference here largely follows [32]. The expression for the likelihood function depends on the noise model. In gravitational wave astronomy we typically assume Gaussian noise and this leads to a likelihood similar to the following expression:

$$\mathcal{L}(d|\theta) = \frac{1}{2\pi\sigma^2} \exp\left(-\frac{1}{2} \frac{|d - \mu(\theta)|^2}{\sigma^2}\right), \quad (3.18)$$

with the normalization constant for a 2-dimensional Gaussian because the data is typically complex. Here $\mu(\theta)$ denotes the value of a gravitational wave template with certain parameters θ and σ is the standard deviation of the detector noise.

The prior $\pi(\theta)$ gives some prior belief about the parameter values θ and there is freedom in choosing this. What choice to make will depend on the situation. In the case of neutron stars, for example, we have some beliefs about their possible range of masses. When not much is known about a parameter this can be expressed by using a uniform prior, giving equal probability to all values.

In gravitational wave astronomy we often only want to look at one or two parameters at a time, for example the component masses. In this case the parameters we are not interested in are called nuisance parameters. The process of eliminating the nuisance parameters is called marginalization and it is done by integrating over them. This results in the marginalized posterior:

$$p(\theta_i|d) = \int \left(\prod_{k \neq i} \theta_k \right) p(\theta|d). \quad (3.19)$$

This can be described as taking weighted results over all values of the nuisance parameters with weights proportional to the posterior probability of the nuisance parameter

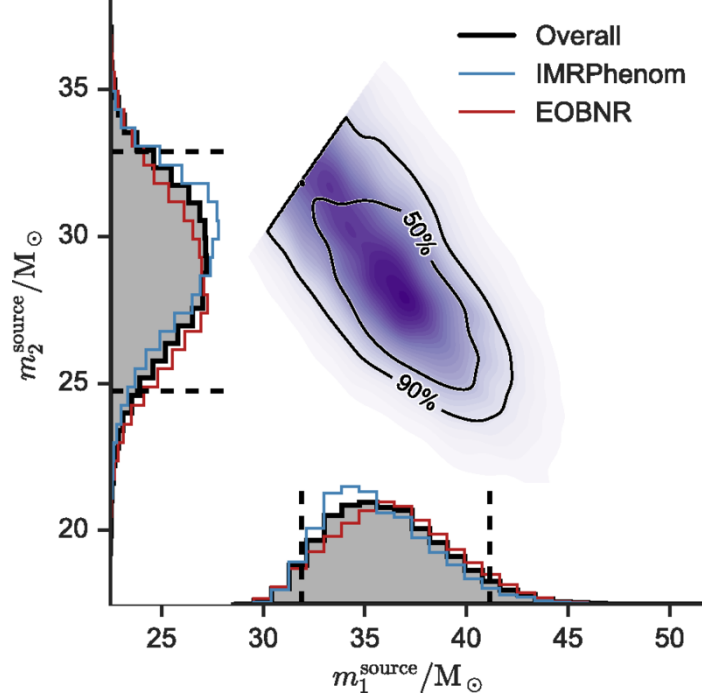


Figure 3.3: Posterior distribution for the component masses of GW150914 by using Phenom or EOBNR waveforms. Source [33].

values. Equation 3.19 can also be expressed as

$$p(\theta_i|d) = \frac{\mathcal{L}(d|\theta_i)\pi(\theta_i)}{\mathcal{Z}}, \quad (3.20)$$

where $\mathcal{L}(d|\theta_i)$ is called the marginalized likelihood and is given by

$$\mathcal{L}(d|\theta_i) = \int \left(\prod_{k \neq i} d\theta_k \right) \pi(\theta_k) \mathcal{L}(d|\theta). \quad (3.21)$$

Figure 3.3 shows the posterior distribution of the component masses of GW150914 after marginalizing over other parameters. It also shows contours of 50% and 90% credible intervals.

This posterior probability can be written as

$$P(\theta|s) = A\pi(\theta) \exp \left(\frac{1}{2}(h(\theta)|s) - \frac{1}{4}(h(\theta)|h(\theta)) \right), \quad (3.22)$$

as derived in [48]. Here $(...|...)$ denotes the inner product as in equation 3.11 and $h(\theta)$ is the waveform for parameters θ . The signal measured by the detector is denoted as s and A is a normalization constant.

For a given signal one could thus produce many waveforms $h(\theta)$ for varying values of θ to produce the posterior probability distribution. After Marginalizing over nuisance parameters images like figure 3.3 can be produced. The problem is that the parameter space is very large. When considering the 15 parameters to describe a binary black

hole, even taking a very coarse grid of 10 points per parameter will already require producing 10^{15} waveforms, which is not practically feasible. This problem is addressed by appropriate stochastic sampling methods like Markov chain Monte Carlo.

3.3.3 Markov chain Monte Carlo

Markov chain Monte Carlo [49, 50] methods can be used to draw samples from a probability distribution. An arbitrary point, also called *walker*, in the parameter space is taken and then this makes a stochastic walk through the parameter space. When the walker is at a point x , a nearby point x' will be selected according to the proposal distribution $g(x'|x)$. Then this nearby point, the *proposal*, is accepted with a probability $A(x'|x)$ that has to satisfy the equation

$$\frac{A(x'|x)}{A(x|x')} = \frac{P(x')g(x|x')}{P(x)g(x'|x)}. \quad (3.23)$$

Here $P(x)$ needs to be proportional to the probability at point x , which means it is not necessary to evaluate the normalization constant. This is important because evaluating the normalization constant can often be too computationally expensive to be feasible. A common choice for $A(x'|x)$ is the Metropolis choice:

$$A(x'|x) = \min \left(1, \frac{P(x')g(x|x')}{P(x)g(x'|x)} \right). \quad (3.24)$$

When the proposal is accepted the walker will move to the new point in the parameter space and the new point is added to the list of drawn samples. If the point is not accepted the walker stays at the same point, which is also again added to the list of samples. Obviously successive points drawn will be correlated as they will be close to each other in the parameter space. If the algorithm is run for a sufficient amount of time however, the drawn samples will be distributed as the distribution $P(x)$.

This method can be used to make the distribution of $P(\theta|s)$ from equation 3.22, without evaluating the normalization constant A . For each unique point that is sampled in the parameter space a waveform $h(\theta)$ will have to be computed. To produce the distribution one will typically still need a very large amount of points, on the scale of 10^7 or higher. For this to be practically possible it is essential to have an efficient method of producing waveforms.

3.4 Waveform models

Because there is no analytical solution to the 2-body problem in general relativity, one will have to use numerical methods to create waveform models for binary black holes. There are various techniques for creating the waveforms that are used in gravitational wave data analysis. The choice of which technique to use depends on the purpose and on the parameters of the system. This work focuses on similar mass (i.e. no extreme mass ratio inspirals, discussed in section 5.1.3) binaries and this section gives

an overview of the most important methods for the computation of waveforms for these systems.

3.4.1 Numerical Relativity

The most obvious way of creating waveforms is by solving the Einstein field equations numerically for a given system. This is indeed the most accurate method of acquiring waveforms, but the big drawback is its enormous computational cost on the scale of 10^5 to 10^6 core hours for a single waveform. Because of the computational cost the number of available numerical relativity waveforms is very limited and this also limits its practical applications. An important purpose of them is the testing and calibration of other, more efficient techniques of producing waveforms.

Numerical relativity waveforms typically cover only the last ~ 20 orbits, so those at the highest frequency. Extending the waveforms to lower frequencies means getting a lot more orbits and this drastically increases the computational cost. This all means that there are very few numerical relativity waveforms available and that they are very short, which makes the use of them impractical for procedures such as parameter estimation. Fortunately various methods have been developed to produce waveforms more efficiently. Producing these waveforms is generally challenging, but it can become increasingly difficult for certain parameters. Larger mass ratios, larger spins (also depending on their direction) and larger inclination (where 0 means face-on) make effective waveform production more difficult. The total mass is only a scale factor and doesn't influence the shape of the waveform.

3.4.2 Alternative strategies

The waveforms used in parameter estimation mostly come from three different families, which are all studied in this work. All of the studied models are non-precessing and contain higher modes (beyond (2,2)).

Hybrid surrogate models

Only a few thousand numerical relativity waveforms have been produced and so they cover only a small portion of the very large parameter space. A way to be able to cover a larger portion of the parameter space is to interpolate between the available numerical relativity waveforms. The result is known as a surrogate waveform. A problem with such a surrogate waveform is that it can only have a short length, because it cannot be longer than the numerical relativity waveforms that are used for the interpolation. This can be solved by *hybridizing* the waveform, which means that different methods are used for different parts of the waveform. The final part, i.e. the part where the field is strongest, comes from interpolated numerical relativity waveforms. The part of the wave before that comes from other approximate methods. Fortunately the field is weaker for the earlier inspiral and in this case approximate methods are more accurate. These approximate methods can be a post-Newtonian expansion or the use of an effective one-body formalism. In post-Newtonian methods an expansion is made in velocity v/c that expresses the deviation from Newtonian physics. This is mostly effective when deviations from Newtonian physics are small, i.e. in the earlier inspiral phase. The effective one-body formalism [51] aims to analytically describe

the two-body problem as a single particle moving in an effective metric. This can be more accurate than post-Newtonian waveforms, but it is still quite computationally expensive.

This work analyses the newest generation of hybrid surrogate waveforms, namely NRHybSur3dq8 [55]. It uses a combination of post-Newtonian and effective one-body methods to hybridize the waveforms and produces the (5,5) mode and all modes with $l \leq 4$ except (4,0) and (4,1). It is 3-dimensional (using varying mass ratio and with spins only in the z-direction) and it has been calibrated against waveforms up to mass ratio $q = 8$. It is a time domain waveform (so it needs to be Fourier transformed for parameter estimation) and the waveforms have a finite length. This finite length is because the computational cost of post-Newtonian waveforms increases rapidly when lowering the start frequency.

Effective one-body reduced order models

Contrary to post-Newtonian methods, the effective one-body formalism can be used to describe all phases of the waveform. A model from the newest generation that employs these methods is SEOBNRv4HM [54]. It uses the higher modes (3,3), (4,4), (5,5) and (2,1) and it can be used to accurately produce complete waveforms, but its computational cost is high.

Reduced-order Models (ROM) can be used to produce effective one-body waveforms more efficiently. They have a lower order of accuracy (though the loss of accuracy is very limited), but they are produced much faster.

Along with SEOBNRv4HM a ROM was also presented. This model is much more efficient and it is produced in the frequency domain. It is named SEOBNRv4HM_ROM and unlike the original model it is fast enough to be practical for usage in parameter estimation.

Phenomenological models

An entirely different strategy is the use of phenomenological models. These are models that are made in the frequency domain using analytical expressions, which depend on the parameters of the system. These expressions are found by making a phenomenological ansatz, which is then calibrated against numerical relativity waveforms. The analytical expressions can be quickly evaluated and, again, because the waveforms are already produced in the frequency domain they don't need to be Fourier transformed before using them in parameter estimation.

The used model IMRPhenomXHM [53] is an installment from the most recent generation and the previous generation IMRPhenomHM [52] has also been added for extra reference. IMRPhenomHM was the first model for spinning black holes to include higher modes of the multipole expansion (equation 2.25). Instead of just the dominant (2,2) mode it also contains the higher (3,3), (4,4), (2,1), (3,2) and (4,3) modes. IMRPhenomXHM is from the new PhenomX family of phenomenological models, which also contains the dominant mode-only PhenomXAS [56] and the precessing PhenomXP (only (2,2)) and PhenomXPHM (higher modes) [57]. IMRPhenomXHM is an improved version of IMRPhenomHM, so its performance is expected to be better.

3.4.3 Higher modes

All models used here include higher modes. The relative importance of higher modes changes with the inclination of the system, the total mass and the mass ratio, as described in [48]. Equation 2.25, giving the gravitational wave as a multipole expansion, is repeated here:

$$h_+ - ih_\times = \sum_{l \geq 2} \sum_{m=-l}^l {}_{-2}Y_{lm}(\theta, \phi) h_{lm}. \quad (3.25)$$

The h_{lm} modes do not have any angular dependence here. Instead, the angular dependence is described by the spin-weighted spherical harmonics ${}_{-2}Y_{lm}(\theta, \phi)$. Figure 3.4 shows the angular dependence of these functions. There is equatorial symmetry between $m > 0$ and $m < 0$ and the part above/below the equator shows the functions for positive/negative m . The h_{22} mode has the largest value and its spherical harmonic is at its maximum for face-on systems, where most of the other spherical harmonics are equal to zero. So the dominance of the (2,2) is especially large for face-on systems. When the inclination changes the other modes become more important, as ${}_{-2}Y_{22}$ decreases and (most) other spherical harmonics increase. Thus the strength of different modes strongly depends on the inclination of the system.

Another thing that influences the relative importance of modes is the total mass of the system, as shall be confirmed in the results. This is not because of intrinsic properties of the wave, but because of detector sensitivity. As mentioned before the total mass only sets a scale for waveforms; it doesn't change its shape and so it doesn't change how the different modes are related. It does change the frequency emitted by the system and because the detector sensitivity depends on frequency this means that the detector can put extra emphasis on particular phases of the waveform. Since the relative importance of the different modes changes with the different phases of the waveform this means that higher modes might become more important when changing the total mass of the system.

Finally for a symmetric system there will only be emission from the symmetric modes (even m), so all modes with odd m will be zero. When mass ratio is changed (or to a lesser extent, when asymmetry in spin is introduced) the symmetric modes cannot describe the system completely anymore and modes with odd m will be necessary. This effect becomes stronger as the asymmetry increases.

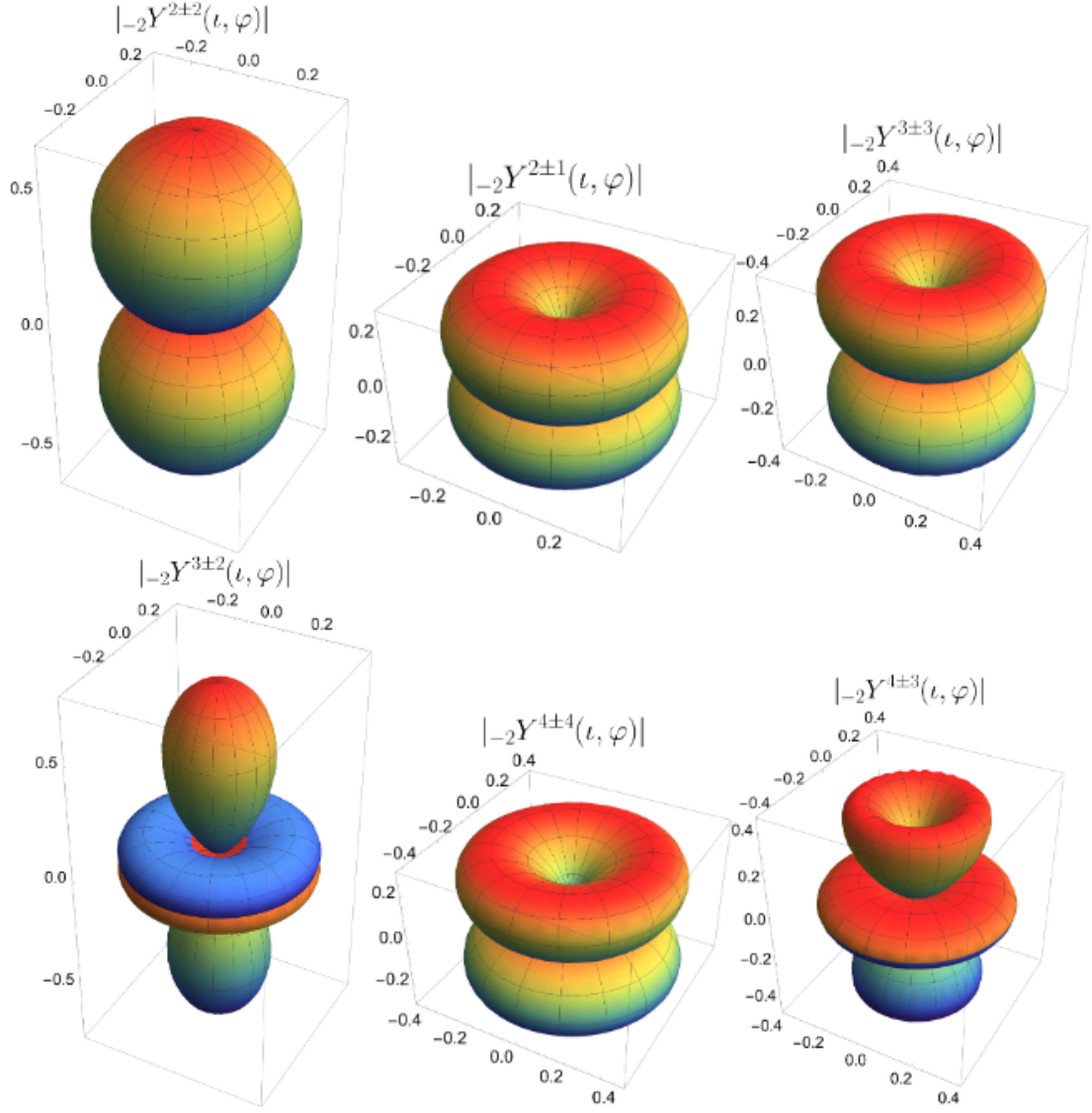


Figure 3.4: The spin-weighted spherical harmonics $_{-2}Y_{lm}$ for the most important modes. Source: [48].

Chapter 4

Einstein Telescope

The Einstein Telescope is a planned ground-based gravitational wave observatory, that is planned to be constructed near Maastricht in the Netherlands or on the Italian island Sardinia and it can be operational in the 2030s. Contrary to current ground-based detectors it will have a triangular shape, which will allow it to effectively work as three interferometers with 60° angles between the arms. This will make its antenna pattern more isotropic than it is for L-shaped detectors, which have some blind or weak directions in their patterns. The telescope will be built a few hundred meters underground, which will reduce gravity gradient and seismic noise [25]. These are the dominant noise sources at low frequencies so building in underground will improve the lower frequency limit compared to current detectors. At 10 km the arms are also significantly longer than current detectors, which will greatly increase its sensitivity. Figure 4.1 shows an artist's impression of what the ET will look like.

The sensitivity is further improved by using mirrors at cryogenic temperatures of about 20 K, which greatly reduces Brownian noise. The sensitivity curve is shown in figure 4.2, which also shows that the ET's sensitivity is a lot better than those of LIGO and Virgo.

4.1 Sources

The compact binary coalescences - the only source of detected gravitational waves so far - that have been observed by LIGO and Virgo can be seen at a much higher SNR by the ET, giving a lot of extra information about the physical nature of these events. Furthermore, the ET could detect these events at a much larger distance as figure 4.3 shows. The extra sensitivity could also enable the ET to observe new types of sources which have not yet been detected by LIGO or Virgo. The various sources discussed here are those in the paper about the science case for the ET [25].

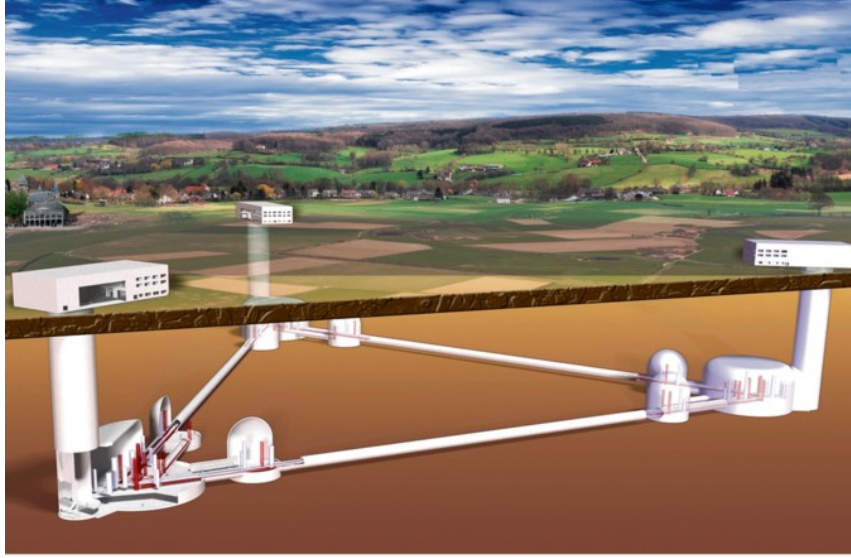


Figure 4.1: Artist's impression of the ET. Image courtesy of Nikhef

4.1.1 Black hole binaries

The ET will be capable of detecting the full population of stellar mass and intermediate mass binary black hole coalescences in the Universe. Information about these events will allow us to answer several questions about their nature. It will give us new data about the earliest population of stars that is not accessible in any other way, which will teach us new things about the history of star formation. Mergers at a smaller distance can be measured at a very high SNR, which will help us to understand the origin and evolution of these systems.

The ET could provide evidence for the existence of primordial black holes, which are black holes that do not have a stellar origin. It is hypothesized that this type of black hole might have formed in the early Universe, where some regions might have been dense enough to undergo gravitational collapse and form a black hole. The ET is expected to detect very large numbers of black hole mergers, which gives great possibilities for statistical analyses. Data on the correlation between star formation and merger rates in the history of the Universe should allow us to disentangle contributions from black holes of stellar origin and primordial origin. Also, the black hole mergers are expected to be found in galaxies, while the distribution of primordial black holes should be related to the distribution of dark matter. Locations of the mergers can be compared to large scale structures in the Universe, which can then teach us about the origin of the black holes. Showing that even a small portion of the black holes has a primordial origin would be very interesting for both astronomy and fundamental physics.

The origin of the supermassive black holes we observe in galactic centers are unknown. There are several hypothesis about their origin and a population of their seeds is expected to exist somewhere in the mass range $10^2 - 10^5 M_{\odot}$. The ET should be able to detect them in a mass range of $10^2 - 10^3 M_{\odot}$. If these will be detected or not will give new information about the seeds.

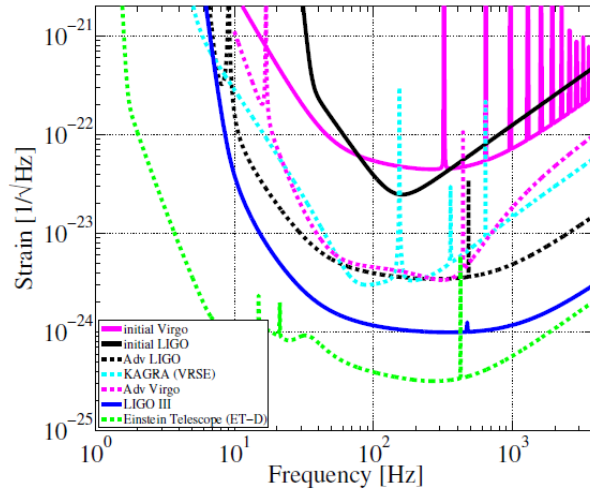


Figure 4.2: Sensitivity curve of the ET compared to several stages of LIGO and Virgo. Image source: [24].

The ET could detect black hole binaries at redshifts $z \approx 10 - 20$. This is before the time where a star could have formed a black hole and thus it would necessarily mean a non-stellar origin. With its frequency range the detector could also observe black holes with sub-solar mass, which would also point to a non-stellar origin. Observing even a single one of such black holes with a non-stellar origin is uncertain but it would be very meaningful.

4.1.2 Neutron stars

The ET should be able to detect neutron star coalescences up to about $z = 3$ at a rate of around 10^5 events per year. Because this also covers the peak star formation rate at about $z = 2$ this means that the vast majority of neutron star binaries is within the detectable range. The high frequency sensitivity of the ET makes it possible to get very accurate measurements of the merger phase of these events. The internal structure of neutron stars remains unknown and these mergers can help us understand them better. This can also greatly help the theoretical field of quantum chromodynamics, which studies the kind of fundamental physics that goes on in neutron stars.

Detecting these neutron star binaries is guaranteed, but there is also a possibility that gravitational waves from a single neutron stars might be observed. If a neutron star has any asymmetries around its rotational axis then they should emit gravitational waves. Data from LIGO and Virgo is already begin used to search for these continuous gravitational waves, but they have not been found yet. Detecting these can give information about the inner structure, formation and evolution of neutron stars.

Besides the continuous waves there is also a chance of detecting transient burst signals from single neutron stars. This could for example come from pulsar glitches, which are small increases in the rotational frequency of a neutron star, which are thought to be caused by interior structure changes. There are more transient events in neutron stars, such as giant magnetar flares. Not much is known about the details of these processes and the emission of detectable gravitational waves is uncertain.

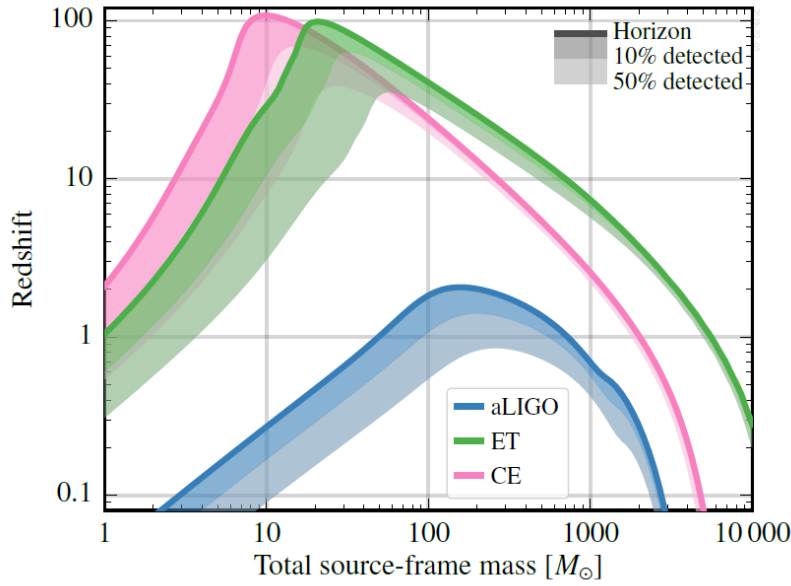


Figure 4.3: Distance of detectable sources as a function of total mass for the ET, Cosmic Explorer (another planned ground-based detector, with an L-shape and 40 km arms) and Advanced LIGO. Image source: [26].

4.1.3 Tests of general relativity

The loudest mergers of neutron stars and black holes can be measured by the ET with a very high SNR. This can provide new tests of general relativity. Comparing the signals of these events to the waveforms that are expected can confirm (or perhaps question) that these objects indeed behave as is predicted by general relativity.

4.1.4 New gravitational wave sources

Other possible sources are supernova explosions. These are not well modelled, which it more challenging to find them, but it is expected that the ET should be able to detect these events within the galactic neighbourhood. The event rate is such that observing them seems realistic, but it is not guaranteed [25]. Similar to the cosmic microwave background for electromagnetic radiation there could be a stochastic background of gravitational waves. The ET could detect this background which will give new knowledge about the early Universe. Finally there is the possibility of detecting entirely new, unexpected sources, as has happened many times before in astronomy when a new window to observe the Universe was opened.

4.2 Noise sources and sensitivity

Over the years several different estimates have been made for the sensitivity curve of the ET. The estimate that currently is in common usage by the community comes from [29]. In that same paper this estimate is referred to as ET-D, whereas previous ones are named ET-B [30] and ET-C [31]. ET-B was the first estimate and it was based on

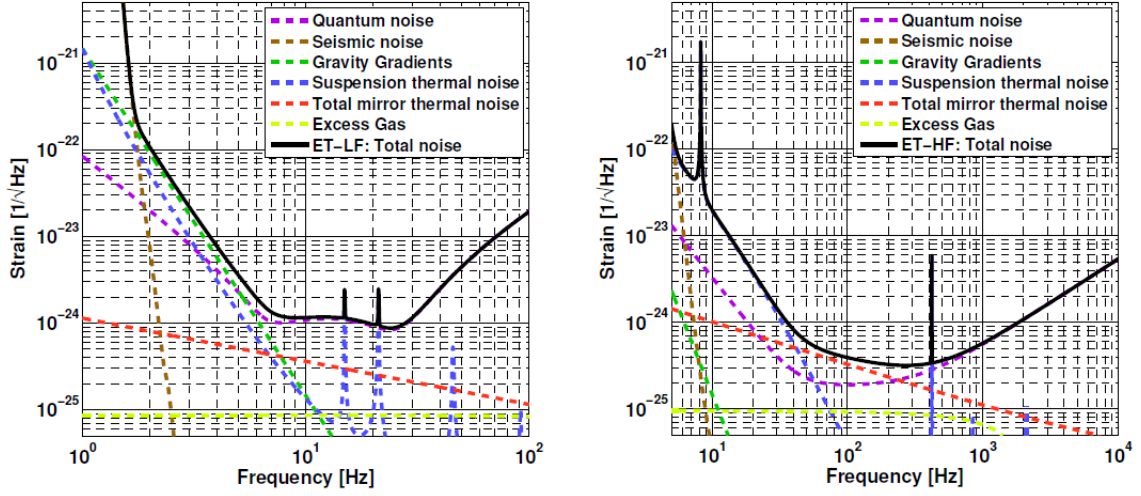


Figure 4.4: Noise budgets for the low frequency (left) and high frequency interferometers of the ET. Source: [29].

a single interferometer in a frequency range of about 1 Hz to 10 kHz. A new estimate took various more realistic technological aspects into account and was based on a new type of design, which was called the xylophone-design. In the xylophone design the detector is composed of two separate interferometer. One uses low laser power and cryogenic mirrors, which makes it best suitable for the low frequencies. The other uses high power and room-temperature mirrors. This channel is used for the high frequency part of the spectrum. The resulting sensitivity curve was named ET-C. Further improvement on ET-C was made by adding new noise sources and making improvements on the noise sources that were already included. This resulted in the ET-D sensitivity curve which shall be used throughout this work.

The main noise sources in ET-D are seismic and gravity gradient noise, quantum noise and thermal noise.

4.2.1 Seismic noise and gravity gradient noise

Seismic effects are the dominant noise sources at low frequencies. They cause noise through two different processes. Seismic waves can move the suspension systems and this is referred to as *seismic noise*. The seismic waves will also cause fluctuations in density around the detector, which causes perturbations in the gravitational forces acting on the systems. The noise caused by this is called *gravity gradient noise*. The seismic noise can be reduced by using seismic isolation systems. The gravity gradient noise can only be reduced by placing the detector in a more quiet environment, which is why the ET is proposed to be built underground.

4.2.2 Quantum noise

The quantum noise is composed of photon shot noise at high frequencies and photon radiation pressure at low frequencies. Shot noise is a consequence of the discrete nature

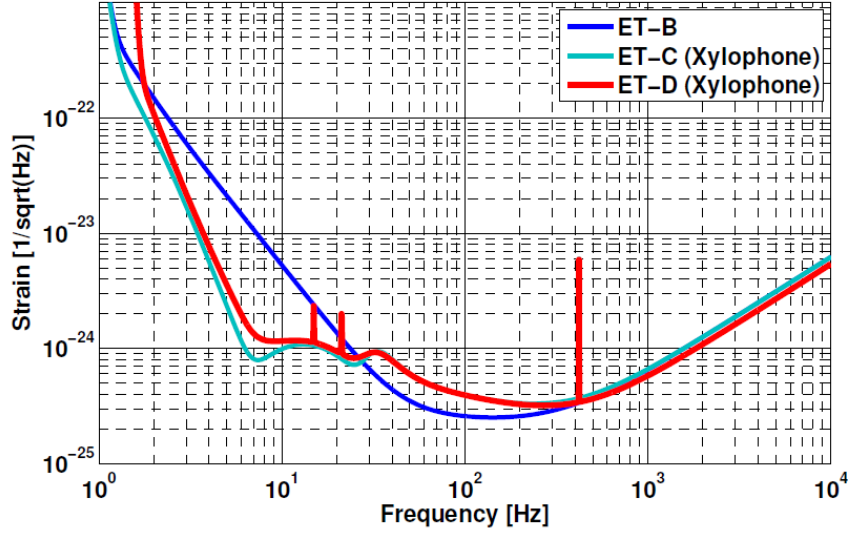


Figure 4.5: Total noise from the different ET sensitivity studies. Source: [29].

of photons, which means that their arrivals can be described as a Poisson process and are subject to its associated noise. Photon radiation pressure noise is noise that is caused by the momentum of the photons coming from the laser, which causes slight movement of the mirrors.

Now the shot noise can be reduced by increasing the laser power, whereas the photon radiation pressure noise can be reduced by decreasing the laser power (and vice versa of course). Since these two types of noise occur at the different ends of the frequency spectrum this led to the idea of the xylophone-design of ET-C, which uses two different interferometers. One of them uses cryogenic mirrors and low power and this one probes the low frequencies, since it reduces the radiation pressure which occurs at lower frequencies. The other uses room temperature mirrors and high power, which reduces the shot noise and because of that this interferometer can be used for the higher frequencies. The noise budgets for both interferometers can be seen in figure 4.4.

4.2.3 Thermal noise

Brownian motion causes noise, because of movement of the test mass itself and of its suspension. At high frequencies the noise does not play a significant role, but at 1 Hz to 10 Hz it is significant, with suspension noise being the main contributor. It can be significantly reduced by using a cryogenic mirror, as is already being done at KAGRA and this will also be used in the low frequency channel (for the higher frequencies it's not necessary because the thermal noise is less important there) of the ET. Even with the cryogenic mirrors the thermal noise is still important as can be seen in figure 4.4.

Finally figure 4.5 shows the total noise budgets for different studies of the ET sensitivity.

Chapter 5

LISA

All gravitational waves that have been observed to date have been detected using ground-based interferometers. The observatories used that have been used in detections so far are Virgo and the two sites of LIGO. The recently completed KAGRA interferometer in Japan is expected to join this list in the near future. These kind of detectors are designed to observe in the range of about 10 Hz to a few kHz [5], where the lower limit is caused by terrestrial gravity noise. There are some concepts for terrestrial detectors in the range 0.1 Hz-10 Hz, but these still face many technical challenges to overcome [6].

The only way of opening the frequency window of about 10^{-4} to 1 Hz seems to be a space-based interferometer, where the terrestrial gravity noise will of course play no role. There are many interesting sources in this frequency range (discussed in section 5.1), and so there are various projects for an observatory in space. The Laser Interferometer Space Antenna (LISA) is planned to be launched in 2034 was the first gravitational wave detector to be proposed [7]. It is an interferometer with 2.5 million km arms, with sensitivity in the frequency range of below 10^{-4} Hz till about 1 Hz. There are some other projects that aim for a launch in the 2030s, though LISA is in the most advanced stage. Examples of other projects are the Chinese Taiji [7], which is similar to LISA at an arm length of about 3 million km, the also Chinese TianQin [9], which will explore about the same frequency range at arm lengths of 10^5 km, and the Japanese DECIGO [8], which will fill in the gap between ground- and other space-based detectors by probing the frequency range between 0.1 Hz and 10 Hz, using arms of 100 km.

LISA will be a constellation of three spacecraft in an equilateral triangle with sides of 2.5 million km. It will trail the orbit of the Earth around the sun by about 20° , with an inclination of 60° to the ecliptic plane, as seen in figure 5.1.

The goal of LISA is to measure changes in the distance between the spacecraft that are caused by gravitational waves, so it is important to avoid any accelerations caused by other effects such as solar wind. To do this LISA will use so-called drag-free spacecraft, which consist of an outer spacecraft and a *test mass* which flies freely inside of

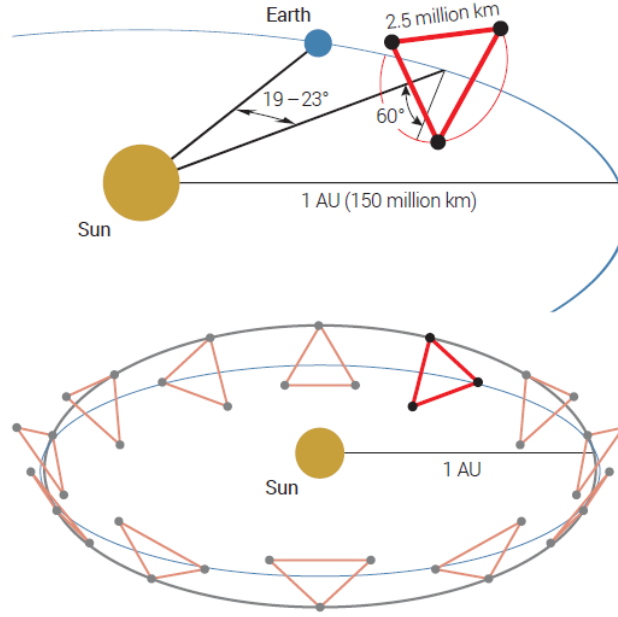


Figure 5.1: Depiction of LISA orbit. Source: [2].

it. The aim is to have the test mass follow a geodesic path (only affected by gravity). The outer spacecraft will float around it and it will be influenced by other forces such as solar wind, which will cause it to move relative to the test mass. This relative motion is monitored and the outer spacecraft will use thrusters to adjust its position if necessary, so that the test mass can continue its geodesic path.

The techniques used to keep the test mass drag-free and several other technologies used in LISA were tested with the LISA Pathfinder mission. The LISA Pathfinder was a spacecraft that was launched in 2015. It uses instruments that are similar to those used by LISA, but it uses a 38 cm arm [10], with two test masses inside a single spacecraft, instead of the 2.5 million km arms of LISA. The relative motion, caused by unwanted accelerations, of the test masses was measured during the operational part of the mission, which lasted from March 1, 2016 until June 30, 2017 [11]. Many technologies used in LISA could be tested in this way and the results of the mission were far better than the requirements, meaning the LISA mission is feasible [11]. Results can be seen in figure 5.2.

In 2017, after the first detection and when it was clear that LISA Pathfinder had met its requirements, the current LISA proposal [2] was accepted.

5.1 Sources

LISA will open up a new frequency window in gravitational wave astronomy. Many interesting sources to which ground-based observatories are not sensitive can be detected by LISA. This section gives an overview of these sources as described in the

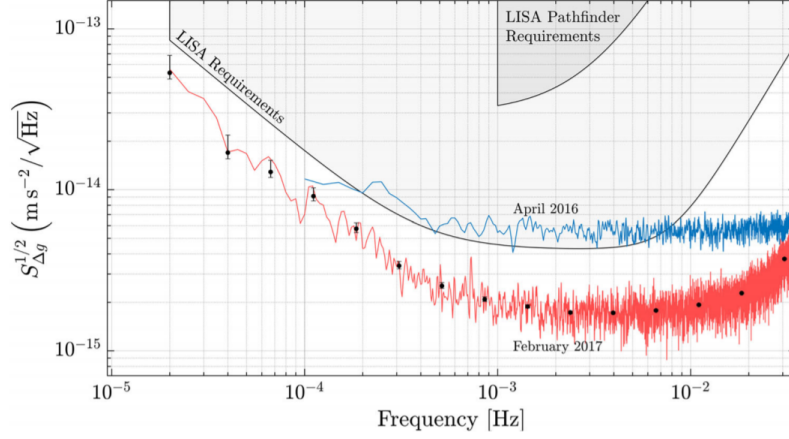


Figure 5.2: Results of the LISA Pathfinder mission. The blue line is the amplitude spectral density of the noise measured by LISA Pathfinder in April 2016 [12], the red line is the noise measured in February 2017. The results in 2017 are better because of residual gas being vented into space and better understanding of other noise sources [11]. The image also shows the mission requirements, which were far exceeded. Image source: [11].

LISA proposal [2]. Figure 5.3 shows an overview of the predicted signals from some of these sources.

5.1.1 Galactic binaries

A large fraction of stars in the galaxy are part of a binary system, in which relatively close stars orbit around their center of mass. Binary systems of dense, compact components (white dwarfs, neutron stars and stellar mass black holes) can interact strongly enough to emit gravitational waves that can be detected by LISA. The frequency of the gravitational waves emitted are twice the orbital frequency of the system. Systems that are more massive and with a smaller separation will thus have a lower frequency and will be louder as measured by LISA. Some systems that should be detectable for LISA have already been discovered through electromagnetic radiation ; these are called *verification binaries*. At least around 15 have already been discovered that should have a good SNR for a four year LISA mission [13], and this number could still increase before LISA's launch. Some of them are also shown in figure 5.3.

The number of low frequency binaries is actually expected to be so high that individual systems cannot be resolved and can be considered as a noise source. These can also be seen in figure 5.3. It is estimated that LISA can resolve approximately 25.000 individual binaries [2], which will give a lot of new knowledge about the mass, spatial and period distributions of these systems.

5.1.2 Massive black holes

Many large galaxies have a massive black hole in their centre with masses ranging from about $10^5 M_{\odot}$ up to $10^9 M_{\odot}$. The formation process of these black holes is still

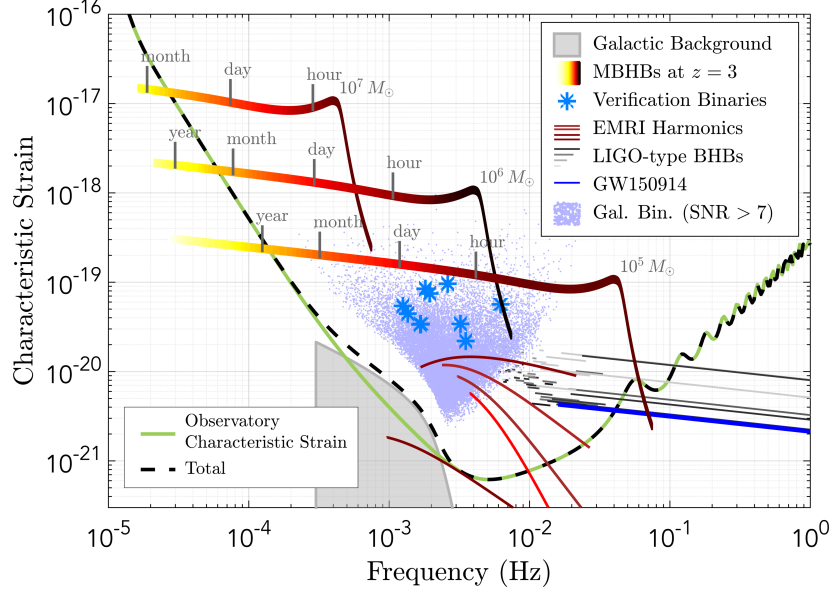


Figure 5.3: LISA sensitivity curve compared with several sources as described in section 5.1. Source: [2].

unknown. Several possibilities for their *seeds* are presented in [14]. It discusses three categories for the seeds: light seeds formed in the very young Universe ($M_{BH} \approx 100 - 600 M_{\odot}$, $z \approx 20 - 50$), intermediate seeds at a later time ($M_{BH} \approx 10^3 M_{\odot}$, $z \approx 10 - 15$) or heavy seeds, formed later again $M_{BH} \approx 10^4 - 10^6 M_{\odot}$, $z \approx 5 - 10$. All growing through different physical processes, involving accretion and mergers. Gravitational waves give information about mass, distance and spin of the black holes involved. The spin is influenced in different ways by mergers and accretion so this will give some information about the growing process. Combined with the mass and distance LISA should be able to teach us a lot about the origin of massive black holes.

Figure 5.4 shows the SNRs for different parameters of black hole mergers, along with some points showing mission requirements from the LISA proposal [2]. Several of these requirements are related to massive black hole mergers. The point marked MR2.1 in the figure is related to the objective to be able to detect mergers for masses between the scale of $10^3 M_{\odot}$ and $10^5 M_{\odot}$, with redshift $z \approx 10 - 15$. The measurement of mass and luminosity distance needs to have a fractional error of about 20% to be able to distinguish between different models of massive black hole formation.

MR2.2 concerns the study of the growth mechanism of massive black holes since the time of the earliest quasars (extremely luminous objects, consisting of a massive black hole with an accretion disk at the center of a galaxy). The strongest requirement set for the LISA mission to study these objects is to be able to accurately (error better than 0.1 for the dimensionless spin) measure the spin of the largest black hole of a system of total mass $10^5 M_{\odot}$, mass ratio of $q = 0.2$ at a distance of $z = 3$. To measure this a large SNR of about 200 is necessary.

Another goal of LISA is to allow the observation of electromagnetic counterparts of a massive black hole merger. The requirement set for this is shown by the point MR2.3 and concerns mergers of massive black holes similar to the one in the Milky-Way, at about $10^6 M_{\odot}$ to $10^7 M_{\odot}$, at the epoch of highest star formation at $z \approx 2$. The SNR

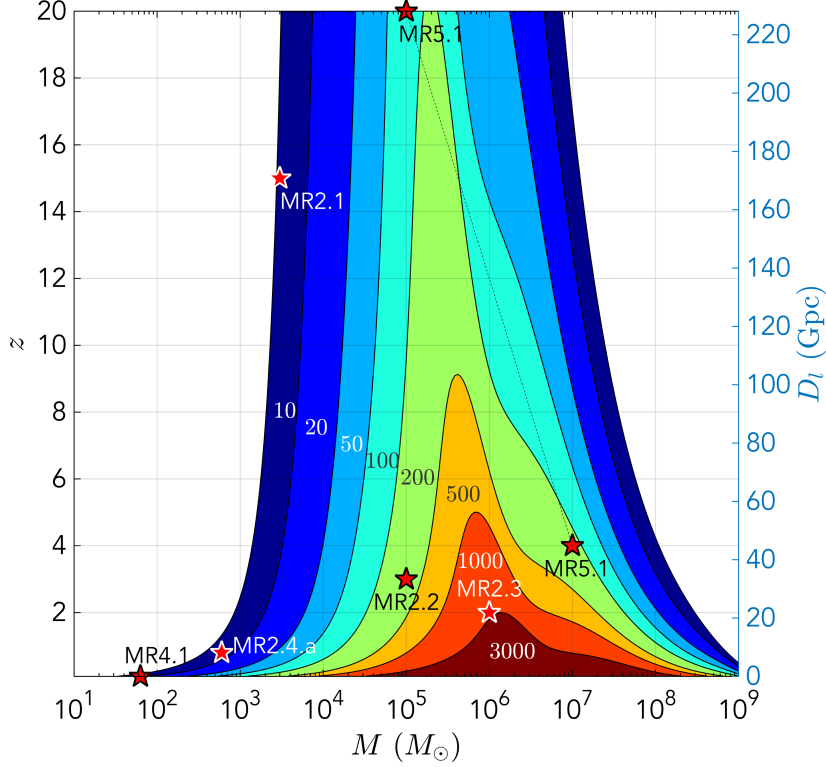


Figure 5.4: SNR for black hole mergers of different mass and distance. The x-axis shows total mass, with a mass ratio of $q = 0.2$. The image is taken from the LISA proposal [2] and also shows some points related to LISA mission requirements. The points shown are discussed in section 5.1.

required is very high because a very precise sky location is necessary to properly conduct the electromagnetic follow-up observation.

MR2.4 is about testing the existence of intermediate mass black holes, which have a mass in the range of $10^2 M_\odot$ to $10^5 M_\odot$, between the range of black holes of stellar origin and the supermassive black holes that we have seen in the centres of galaxies. Recently the first direct detection of such an object was made [62], on the lower end of spectrum at about $M = 150 M_\odot$. The existence of intermediate mass black holes in the rest of the mass range is still debated and so far there are only candidates through indirect observation [15]. Point MR2.4 consists of two parts, MR2.4a concerns the detection of nearly equal massive mergers at a total source-frame mass of about $600 M_\odot$ to $10^4 M_\odot$ at $z < 1$, measuring the component masses at a 30% accuracy, requiring a SNR of about 20. The second requirement, MR2.4b is about detecting a merger of total source-frame mass $10^4 M_\odot$ to $10^6 M_\odot$, of which the lighter has an intermediate mass, at $z < 3$. The aim is to measure the component masses at an accuracy of 10%, which will again require a signal to noise ratio of 20.

5.1.3 Extreme mass ratio inspirals

An extreme mass ratio inspiral (EMRI) is a merger of a massive black hole (about $10^5 M_\odot$ to $10^6 M_\odot$) at a galaxy centre with a stellar mass (a few tens M_\odot). These events can give a lot of interesting information, as discussed in [16]. EMRIs can be used to

test general relativity in the strong field. The light object can be seen as a test-body in the space-time created by the more massive object. By analysing the gravitational waves emitted one can test whether this massive object is indeed a Kerr black hole acting as predicted by general relativity.

The gravitational waves emitted by an EMRI can contain a lot of information about the parameters of the massive black hole that would be very difficult to obtain otherwise. These parameters can give new astrophysical information. The spin of the massive black hole would, for example, give new knowledge about its formation. High spin could indicate an origin in a gas accretion disc, low spin could mean a sequence of mergers with lighter objects coming from random directions.

5.1.4 Stellar Origin Black Holes

Stellar Origin Black Hole (SOBH) inspirals are expected to be the first sources for multi-band gravitational wave astronomy. The observation rate of SOBHs from ground-based detectors indicates that we could observe up to a few hundred of these events during the LISA lifetime [17]. Some of these will enter the LIGO band several weeks later. LISA could thus predict the mergers a few weeks in advance and could determine the time and location with uncertainties below 10 s and 1 deg². This allows the pointing of telescopes at the event, so that it could be observed both through gravitational waves with ground-based detectors and through electromagnetic waves.

5.1.5 Nature of gravity and black holes

Massive black hole binaries and EMRIs with a very high SNR can be used to study general relativity in the strong field regime. The waveform of a massive black hole binary can be used to study if they indeed behave as predicted by general relativity. Sensitivity requirements for studying this are shown as MR5.1 in figure 5.4.

Waves from EMRIs with high SNR can be used to study the multipolar structure of MBHs. It should be possible for LISA to get very accurate measurements of the parameters of EMRIs which can be used to study the deviation from a Kerr black hole quadrupole moment. LISA can also test the presence of dipole radiation, which would be beyond general relativity.

Propagation properties of gravitational waves can be inferred from EMRIs and MBHBs. These can be used to study the dispersion relation of gravitational waves, to find an upper limit for the mass of the graviton (the hypothesized quantum of the gravitational field, like the photon is for the electromagnetic field) and possible violations of Lorentz invariance.

Measurements of MBHBs can be used to constrain masses of certain particles or fields predicted by dark matter models. The inspiral of a solar mass object into an intermediate mass black hole (mass below a few M_{\odot}) can be investigated to analyse possible deviations that are caused by the presence of dark matter.

5.1.6 Measure the rate of expansion of the Universe

Gravitational waves can be used to measure the value of the Hubble parameter. Standard sirens, objects for which the absolute distance can be known from the strength of the gravitational wave signal (similar to the so-called *standard candles* in electromagnetic astronomy) be used for this. The redshift may be measured through an electromagnetic counterpart, as in GW170817 [19], but may also be determined from gravitational wave data only [18].

5.1.7 Stochastic gravitational wave background

There are two types of stochastic gravitational wave background radiation. The first comes from compact binaries, which are expected to be very numerous. LISA aims to characterise the spectrum of this stochastic background. Then there is also background radiation from the very early Universe, analogous to the cosmic microwave background of electromagnetic radiation. The gravitational wave background will allow us to look even further back however, since the Universe only became transparent to electromagnetic radiation after about 400.000 years. Looking back further than that will be very valuable for testing competing theoretical models of fundamental physics and cosmology.

5.1.8 Gravitational wave bursts and unforeseen sources

LISA will open up a new window to the Universe and there might be new, perhaps unexpected sources to discover. A potential new discovery would be the cosmic string. Cosmic strings are predicted by various theories of the early Universe. Cusps and kinks in these objects could create gravitational wave bursts, which LISA might be able to detect [20]. This would be of large importance to theoretical physics. Various other unexpected or perhaps even completely unknown sources could be detected.

5.2 Time Delay Interferometry

Ground-based interferometers like LIGO and VIRGO have arms that are of very precisely equal length. This allows them to measure with a precision far higher than frequency noise in the laser would normally allow them to. This is because the frequency noise is exactly the same in both arms and the noise cancels out. For LISA however the arm lengths only stay equal to about 1% and this noise will no longer be automatically cancelled. This noise is much larger than all other noise sources and would completely overwhelm the signal if not cancelled somehow.

Fortunately the noise can still be removed through some particular linear combinations of time-shifted Doppler observables in a procedure called Time-Delay-Interferometry (TDI), first introduced in [21]. The three LISA spacecraft are numbered 1,2 and 3 and then the Doppler observable is denoted as y_{sr} , with s for *sending* and r for *receiving*. The expression for y_{sr} was first derived in [58] and can be written as

$$y_{sr} = \frac{1}{2} \frac{n_l \otimes n_l}{1 - k \cdot n_l} : [H(t - L - k \cdot p_s) - H(t - k \cdot p_r)]. \quad (5.1)$$

Here n_l is the unit vector pointing from the sending to the receiving spacecraft, k is the wave propagation vector and p_r, p_s are the position vectors of the spacecraft. $A : B$ denotes $A_{ij}B_{ij}$. So y_{31} is the observable from the laser that was sent from spacecraft 3 to spacecraft 1. For time-delayed observables the notation is $y_{sr,nL} = y_{sr}(t - nL)$, where L is the distance between spacecraft, so it is delayed by the travel time between two spacecraft (with $c = 1$).

The laser frequency noise at spacecraft i is denoted as $C_i(t)$. For the observable y_{sr} the laser noise from the sending spacecraft will be measured a time L later, whereas the noise from the receiving spacecraft will be immediately registered. So the noise for y_{sr} is equal to

$$y_{sr}^{laser} = C_s(t - L) - C_r(t). \quad (5.2)$$

So the total signal will be equal a combination of the gravitational wave signal, the laser noise and other noise sources:

$$y_{sr}(t) = y_{sr}^{GW}(t) + y_{sr}^{laser} + y_{sr}^{other}. \quad (5.3)$$

Now a combination is sought that eliminates the laser noise while keeping the gravitational wave signal. There are many possibilities for achieving this. In this case the observables X, Y and Z as in [21] are used:

$$X = y_{31} + y_{13,L} + (y_{21} + y_{12,L})_{,2L} - (y_{21} + y_{12,L}) - (y_{31} + y_{13,L})_{,2L}, \quad (5.4)$$

where Y and Z can be obtained by cyclic permutation $1 \rightarrow 2 \rightarrow 3 \rightarrow 1$. These are the so-called first generation TDI observables and they assume a rigid LISA constellation. Refinements have been made in further TDI generations, which only marginally affect the response to gravitational waves and they shall not be used here. In this case, using equations 5.2 and 5.4, the laser noise for X is explicitly equal to

$$\begin{aligned} X^{laser} &= C_3(t - L) - C_1(t) \\ &\quad + C_1(t - 2L) - C_3(t - L) \\ &\quad + C_2(t - 3L) - C_1(t - 2L) \\ &\quad + C_1(t - 4L) - C_2(t - 3L) \\ &\quad - C_2(t - L) + C_1(t) \\ &\quad - C_1(t - 2L) + C_2(t - L) \\ &\quad - C_3(t - 3L) + C_1(t - 2L) \\ &\quad - C_1(t - 4L) + C_3(t - 3L) \\ &= 0. \end{aligned}$$

A linear combination of X, Y and Z will still cancel the laser noise. As derived in [22], optimal sensitivity to gravitational waves is acquired by the combinations

$$A = \frac{1}{\sqrt{2}}(Z - X), \quad (5.5)$$

$$E = \frac{1}{\sqrt{6}}(X - 2Y + Z), \quad (5.6)$$

$$T = \frac{1}{\sqrt{3}}(X + Y + Z). \quad (5.7)$$

Which shall be used in next section for the LISA response.

5.3 LISA response

When computing the detector response for a compact binary coalescence, there are several difficulties for the case of LISA when compared to ground-based detectors. The signals of LISA will last a lot longer (up to years), so its orientation will change significantly over this time. Also, LISA will be able to measure wavelengths that are shorter than its arm length, which gives some additional challenges when compared to ground-based detectors (for which the arm lengths are much shorter than the measured wavelengths). This discussion of expressions for the LISA response largely follows [4].

First some formalism is introduced. The equation for the multipole expansion (equation 2.25) is repeated here again:

$$h_+ - ih_\times = \sum_{l \geq 2} \sum_{m=-l}^l {}_{-2}Y_{lm}(\theta, \phi) h_{lm}. \quad (5.8)$$

This equation can be split into the real and imaginary parts:

$$h_+ = \frac{1}{2} \sum_{l \geq 2} \sum_{m=-l}^l {}_{-2}Y_{lm}(\theta, \phi) h_{lm} + {}_{-2}Y_{lm}^*(\theta, \phi) h_{lm}^*, \quad (5.9)$$

$$h_\times = \frac{1}{2} \sum_{l \geq 2} \sum_{m=-l}^l {}_{-2}Y_{lm}(\theta, \phi) h_{lm} - {}_{-2}Y_{lm}^*(\theta, \phi) h_{lm}^*. \quad (5.10)$$

This allows $h_{+,\times}$ to be written in the Fourier domain as

$$\tilde{h}_{+,\times} = \sum_{l \geq 2} \sum_{m > 0} K_{lm}^{+,\times} \tilde{h}_{lm}, \quad (5.11)$$

where

$$K_{lm}^+ = \frac{1}{2} ({}_{-2}Y_{lm}(\theta, \phi) + (-1)^l {}_{-2}Y_{l,-m}^*(\theta, \phi)), \quad (5.12)$$

$$K_{lm}^\times = \frac{1}{2} ({}_{-2}Y_{lm}(\theta, \phi) - (-1)^l {}_{-2}Y_{l,-m}^*(\theta, \phi)). \quad (5.13)$$

Here the following symmetry relation for the non-precessing case (which is studied in this work) is used:

$$h_{l,-m} = (-1)^l h_{lm}^*. \quad (5.14)$$

Using the notation

$$P_{lm} = P_+ K_{lm}^+ f + P_\times K_{lm}^\times, \quad (5.15)$$

where $P_{+,\times}$ are the polarization tensors. In matrix form P_+ is equal to the diagonal matrix with entries $\{0, 1, -1, 0\}$ and P_\times the anti-diagonal matrix with entries $\{0, 1, 1, 0\}$. The complete signal can now be written as

$$H = \sum_{l \geq 2} \sum_{m > 0} P_{lm} h_{lm}. \quad (5.16)$$

The response to a gravitational wave (equation 5.1) can be split into response for the individual modes, with a transfer function for each term. In the Fourier domain this can be written as

$$\tilde{y}_{sr} = \sum_{l \geq 2} \sum_{m=-l}^l T_{sr}^{lm}(f) \tilde{h}_{lm}. \quad (5.17)$$

This formalism was used in [59] and the transfer function is, in leading order of approximation, equal to:

$$T_{sr}^{lm}(f) = G_{sr}^{lm}(f, t_f^{lm}), \quad (5.18)$$

where

$$G_{sr}^{lm}(f, t_f^{lm}) = \frac{i\pi f L}{2} \text{sinc}(\pi f L(1 - k \cdot n_l)) \exp(i\pi f(L + k \cdot (p_r + p_s))) n_l \cdot P_{lm} \cdot n_l, \quad (5.19)$$

P_{lm} is defined as in equation 5.15 and

$$t_f^{lm} = -\frac{1}{2\pi} \frac{d\Psi^{lm}}{df}, \quad (5.20)$$

with Ψ^{lm} being the phase of h_{lm} .

The time-delay interferometry observables as defined in equations 5.5, 5.6 and 5.7 can, in the Fourier domain, be written as

$$\tilde{a} = (1 + z)(\tilde{y}_{31} + \tilde{y}_{13}) - \tilde{y}_{23} - z\tilde{y}_{32} - \tilde{y}_{21} - z\tilde{y}_{12}, \quad (5.21)$$

$$\tilde{e} = \frac{1}{\sqrt{3}} [(1 - z)(\tilde{y}_{13} - \tilde{y}_{31}) + (2 + z)(\tilde{y}_{12} - \tilde{y}_{32} + (1 + 2z)(\tilde{y}_{21} - \tilde{y}_{23})], \quad (5.22)$$

$$\tilde{t} = \frac{\sqrt{2}}{\sqrt{3}} [\tilde{y}_{21} - \tilde{y}_{12} + \tilde{y}_{32} - \tilde{y}_{23} + \tilde{y}_{13} - \tilde{y}_{31}]. \quad (5.23)$$

Here a factor z is used for a time delay L , i.e. $z \equiv \exp 2i\pi fL$. The variables have been rescaled according to

$$\tilde{a}, \tilde{e} = \frac{\exp(-2i\pi fL)}{i\sqrt{2}\sin(2\pi fL)} \times \tilde{A}, \tilde{E}, \quad (5.24)$$

$$\tilde{t} = \frac{\exp(-3i\pi fL)}{2\sqrt{2}\sin(\pi fL)\sin(2\pi fL)} \times \tilde{T}. \quad (5.25)$$

The PSDs for these channels can be written as

$$S_n^a = S_n^e = 2(3 + 2\cos(2\pi fL) + \cos(4\pi fL))S^{pm}(f) + (2 + \cos(2\pi fL))S^{op}(f), \quad (5.26)$$

$$S_n^t = 4\sin^2(2\pi fL)S^{pm}(f) + S^{OP}(f). \quad (5.27)$$

Finally a strain-like noise PSD for these TDI observables is defined as

$$S_h^{a,e,t}(f) = \frac{S_n^{a,e,t}(f)}{(6\pi fL)^2}. \quad (5.28)$$

This was done assuming a rigid constellation and perfect noise cancellation. Some local differences in sensitivity are expected for a more realistic model. A further assumption is to use the low-frequency limit, where the wavelength is much smaller than the arm length. This means that the delay $z \approx 1$ and since the travel time of a wave along a link no longer needs to be considered there will be link reversal symmetry: $y_{ij} = y_{ji}$. Plugging this into equations 5.21, 5.22 and 5.23 yields

$$\tilde{a} \approx 4\tilde{y}_{31} - 2\tilde{y}_{23} - 2\tilde{y}_{12}, \quad (5.29)$$

$$\tilde{e} \approx 2\sqrt{3}[\tilde{y}_{12} - \tilde{y}_{23}], \quad (5.30)$$

$$\tilde{t} \approx 0, \quad (5.31)$$

So \tilde{t} doesn't have to be considered in this case and in equation 5.28 only the cases for \tilde{a} and \tilde{e} need to be taken into account.

Using this treatment with the assumptions that were mentioned LISA can be treated as two LIGO-type detectors that are rotated by $\pi/4$. The response to $h_{a,e}$ is then similar to the LIGO response to $h_{+,\times}$, but using the effective PSD from equation 5.28. The approximations mean that it can only be used for frequency up to about 10^{-2} Hz.

Part II

Results

Comparison of inspiral, merger and ringdown sensitivities

Different detectors have different sensitivity curves and thus they may emphasize different parts of the waveform. Figure 6.1 shows the sensitivity curves for the detectors used in this work and waveforms of some systems with a typical mass they could detect (IMRPhenomXHM, (2,2) mode waveforms). One detector might have a relatively better sensitivity in the frequency range where, for example, the merger occurs. To make a comparison between the detectors a procedure called *whitening* is used. Furthermore, LISA operates in a different frequency and mass range, so to make a comparison between LISA and the ground-based detectors one will have to use some kind of scaling factor. The choice was made to use the ratio between the characteristic frequencies (the frequency where the noise PSD is at its minimum) of aLIGO and LISA as the scaling factor, giving a value of 3.1×10^4 . It is emphasized that this is somewhat arbitrary so the scaled masses cannot be strictly considered as equivalents.

6.1 Whitening

Parts of the waveform where a detector has good sensitivity will be emphasized by that detector. To see what a certain waveform would look like (in terms of SNR) for a given detector one can divide, in the frequency domain, the strain of the waveform by the strain of the detector, which is the square root of the PSD. The whitened waveform $\mathcal{W}(f)$ for the polarizations $h_{+,\times}$ can be expressed as

$$\mathcal{W}(f) = \frac{h_{+,\times}(f)}{\sqrt{S_n(f)}}, \quad (6.1)$$

where $S_n(f)$ is the PSD (equation 5.28 is used for the case of LISA). So the waveform will be weighted at each frequency according to how good the sensitivity is at that frequency. The resulting weighted waveform will then be in units of SNR/Hz, so that integrating it over all frequencies yields the total SNR. The image on the left in figure 6.2 shows IMRPhenomXHM (2,2) mode waveforms, one whitened with aLIGO sensitivity and one whitened with LISA sensitivity, using the scaling factor of 3.1×10^4

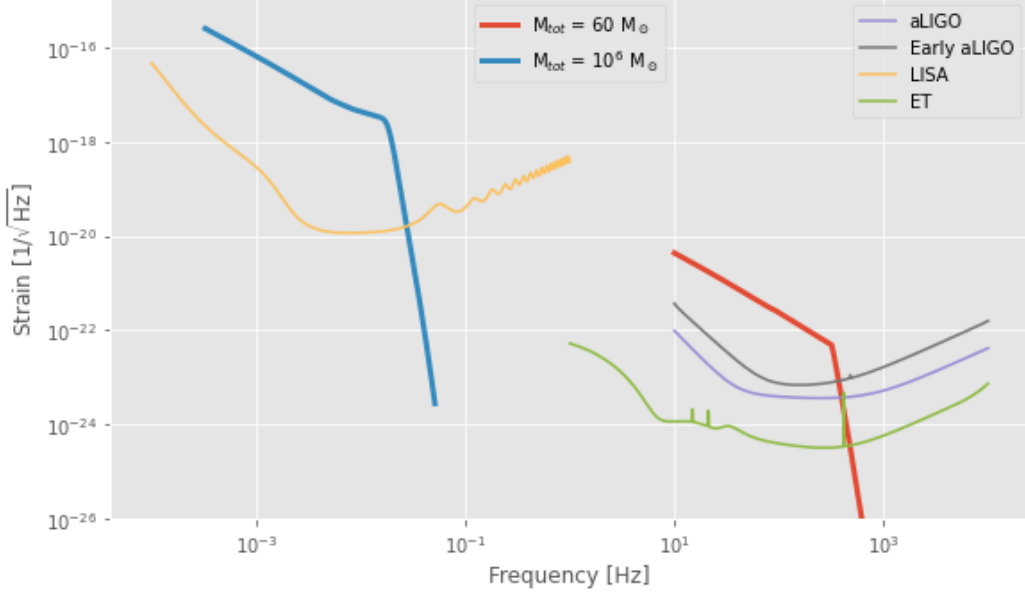


Figure 6.1: Sensitivity curves, also showing waveforms for typical detectable mass.

to convert between aLIGO and LISA. It shows, for example, that for LISA the lower frequencies are reduced more by the whitening, meaning that for LISA the lower frequencies, i.e. the inspiral, are less important than they are for LIGO.

This can also be seen in the time domain plots (image on the right in figure 6.2), where the inspiral is clearly more prominent for LIGO than it is for LISA. This of course also means that the merger and ringdown are more important for LISA than they are for LIGO. This relative importance will vary with the parameters for the waveform.

6.2 Inspiral, merger and ringdown

The first phase of a binary coalescence is the inspiral, which starts at a large separation where the system is slowly losing energy through gravitational radiation. This gradually reduces the separation, so that the binary constituents are spiraling towards each other. The merger is usually said to begin around the time of the innermost stable circular orbit, i.e. the last fully completed orbit. In the merger the black holes plummet into each other. Once they start to overlap the resulting single black hole will finally stabilize in what's called the ringdown.

To compare how much of the total SNR is contained in each of these phases they will have to be distinguished somehow. There are various ways to do this. In this case the transition from merger to ringdown is taken to occur when the waveform is at its peak amplitude. As mentioned before a change in mass does not change the shape of the waveform but only its scale. The time for a waveform can be rescaled to express it in units of mass. This makes it mass independent and this conversion can be made by using

$$t(M) = \frac{t(s)c^3}{GM_{tot}}, \quad (6.2)$$

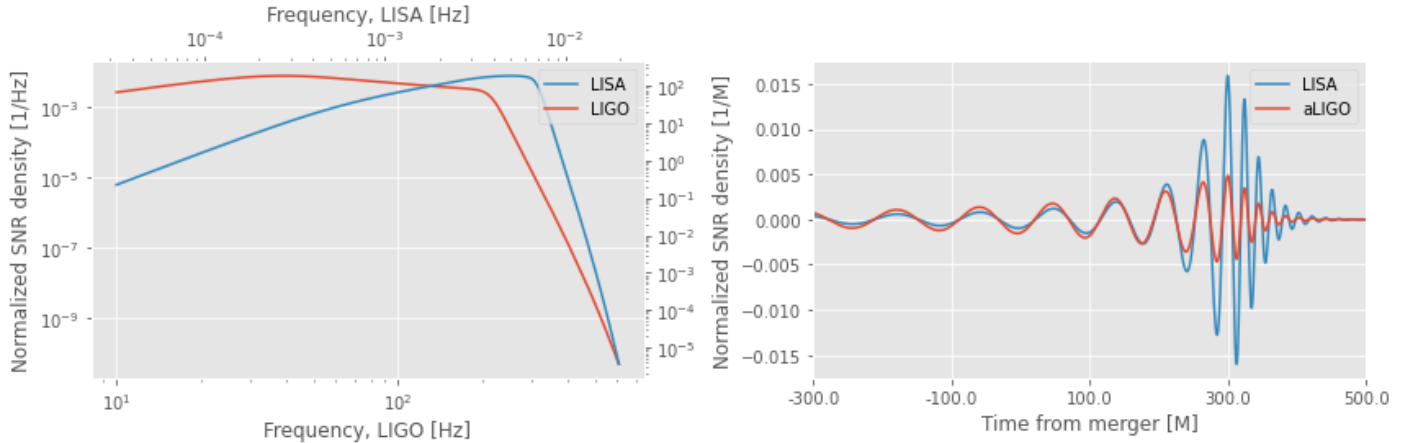


Figure 6.2: Waveform whitened for LIGO ($M_{tot} = 100 M_{\odot}$) and LISA ($M_{tot} = 3.01 \times 10^6 M_{\odot}$), showing the frequency domain (left) and the time domain.

where G is the gravitational constant. The inspiral is then taken to occur a time $150 M$ before the end of the merger. This is a simple, uniform way of distinguishing between inspiral, merger and ringdown. It can be used to give a good impression of how different detectors emphasize different parts of the waveform and how this varies with the mass and spins.

6.3 Results

The results have been produced for three different spin combinations. The spins are taken to be aligned and in the z -direction. The first case is spinless: $\chi_z^1 = \chi_z^2 = 0$. Then large aligned spins are taken at $\chi_z^1 = \chi_z^2 = 0.9$ and finally large antiparallel spins with $\chi_z^1 = 0.9$ and $\chi_z^2 = -0.9$. Aligned spins cause repulsion between the masses, increasing the duration of the inspiral, whereas antiparallel spins cause additional attraction, making the inspiral shorter but stronger.

Spinless

Figure 6.3 shows the SNR ratio of inspiral/merger for different modes and varying mass for the spinless case. This ratio is at its maximum for the low masses for each detector, which could be expected because the inspiral will cover (almost) the entire range of frequencies where the detector has good sensitivity. As the mass is increased the frequencies of the waveform are reduced, so the inspiral phase becomes shorter, whereas the merger moves towards better sensitivities. This causes the ratio between inspiral and merger to decrease. The difference between LIGO and LISA stays within

one order of magnitude as the ratio decreases, but for LISA the ratio is generally smaller (though it should be noted that this comparison depends on the choice for the scaling factor between LISA and ground-based detectors). The ratio for the ET mostly stays around an order of magnitude larger than the others. For the ET the frequency range with relatively good sensitivity is wider than for the other detectors. The inspiral covers a wide frequency range and so the ET will, for a larger range of

masses, get more of its SNR from the inspiral when compared to the other detectors. For some of the modes we can see that ratios sweep up a bit again for the highest masses. This is most pronounced for the (2,1) and (3,2) modes. These modes have a more complicated structure and, especially when the inspiral is very short, some small movement of the peak can have a large effect on the inspiral/merger ratio.

Figure 6.4 shows the SNR ratios between the merger and ringdown phases of the waveform. For LISA and LIGO we can see steadily (albeit a bit noisy at the at the lowest masses) decreasing curves again. In figure 6.3 the ratio also decreases with increasing mass. Some similarities could have been expected since the inspiral, merger and ringdown phase radiate, in that order, at increasing frequency. For the ET the curves in figure 6.4 look a bit more complicated. The ET sensitivity curve has more structure than the others and since the merger and ringdown only cover a small frequency range this structure gives some clearly visible effects.

This just showed the relative importance of the different phases, but the absolute values of the SNR also vary significantly with the mass and modes.

This can be seen in figure 6.5. It shows the detection horizon, which is the maximum distance at which the source can be detected when requiring a minimum SNR of 8 to confirm this detection. The image makes it clear that LISA and the ET cover the entire observable Universe (with a radius of about 14 Gpc) at high SNR for most of their frequency range. To compare the order of magnitude for each mode, the choice was made to show the distance for each mode at the optimal inclination corresponding to this mode, with the exception of the (2,2) mode, which is shown at both the optimal (face-on) and worst (edge-on) inclination. This image would thus be different for a specific inclination; each mode will be multiplied by a constant corresponding to the spherical harmonic for the inclination. For all detectors the face-on (2,2) mode clearly dominates, but when taking it edge-on it can become more comparable, or even smaller, than the (3,3) mode at ideal inclination. The curves look very similar for each of the detectors, when taking into account that the LISA range is a lot wider compared to the width of the peak.

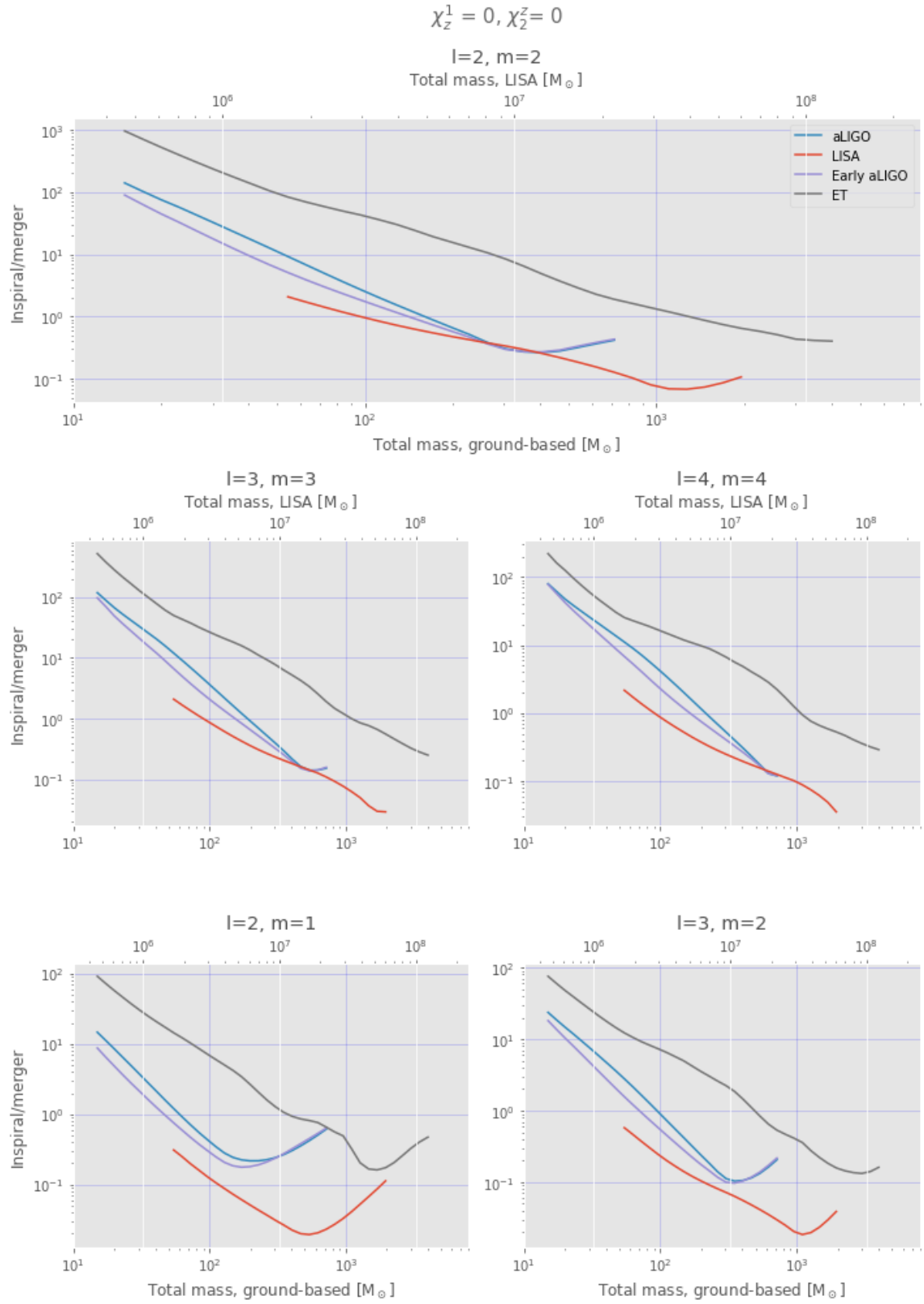


Figure 6.3: SNR ratios of inspiral/merger for spinless case.

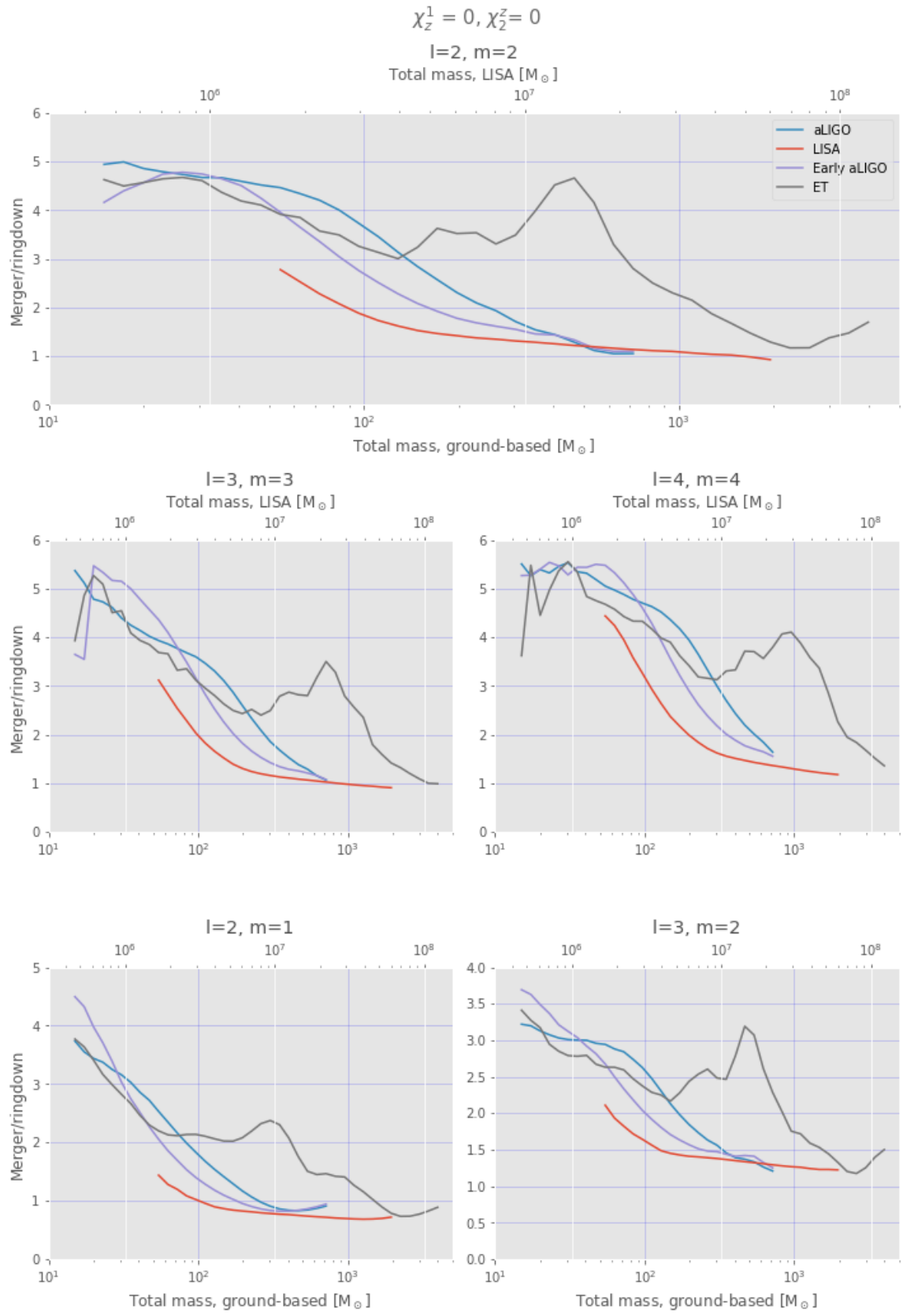


Figure 6.4: SNR ratios of merger/ringdown for spinless case.

$$\chi_z^1 = 0, \chi_z^2 = 0$$

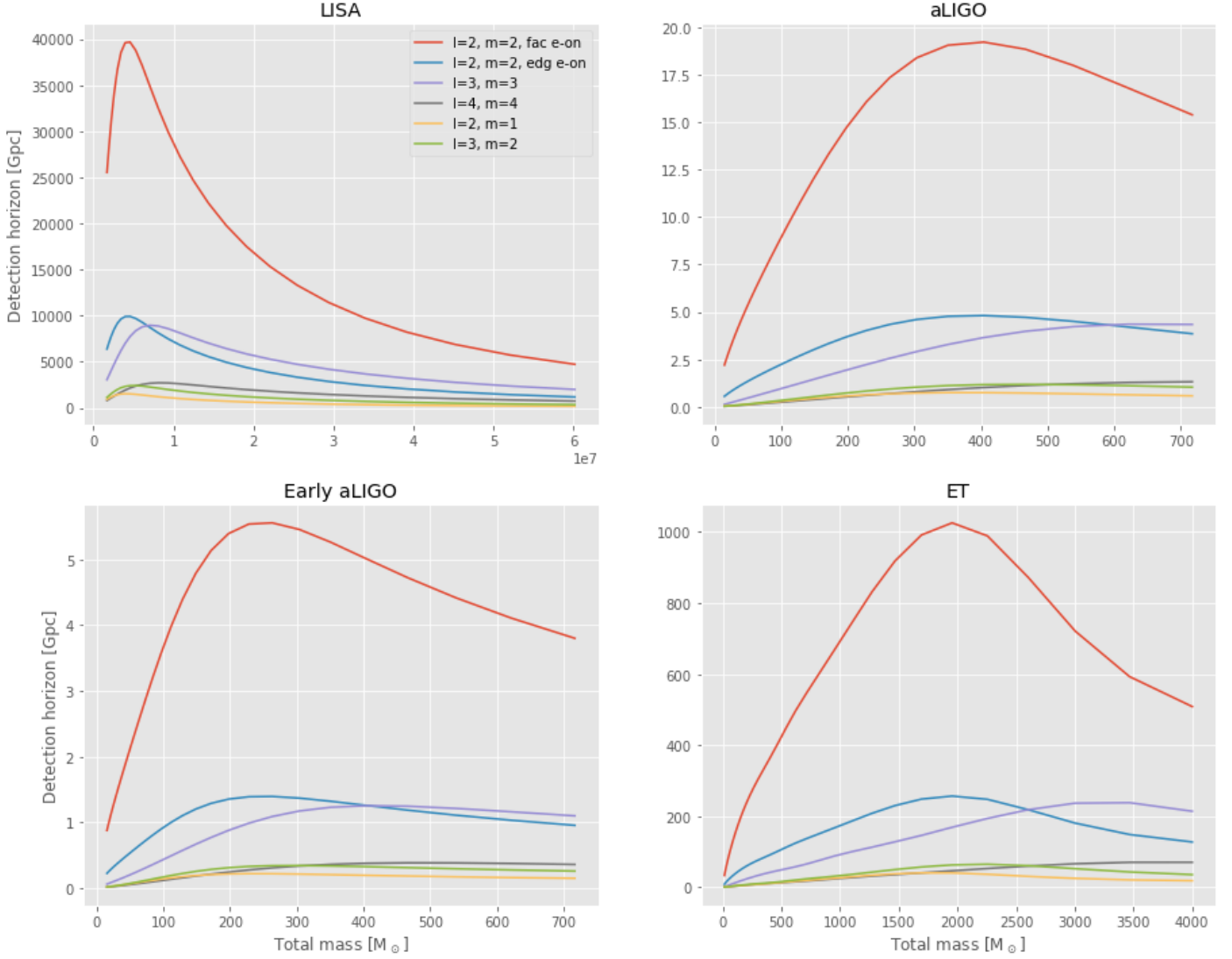


Figure 6.5: Detection horizons for spinless case, assuming a minimum SNR of 8.

Large aligned spins

Figures 6.7, 6.8 and 6.9 show the same results for $\chi_z^1 = \chi_z^2 = 0.9$. The inspiral/merger plots look very similar between both spin cases, but for the merger and ringdown some differences can be seen. The ET curve looks significantly noisier for the (2,2), (3,3) and (4,4) modes. In various cases the curves also make a visible jump. The waveform model is not expected to be as accurate for large spin and higher modes. Artifacts from the Fourier transform can also cause problems. Figure 6.6 shows a time series of the ET around the mass where a jump occurs. As explained before, the end of merger is taken to be at the highest peak in amplitude. Two separate peaks can be seen, with the first being slightly higher. The jump occurs when the second peak becomes bigger and a substantial part of the SNR switches from ringdown to merger. The jump and noise are not too large compared to the absolute values and this plot can still give a

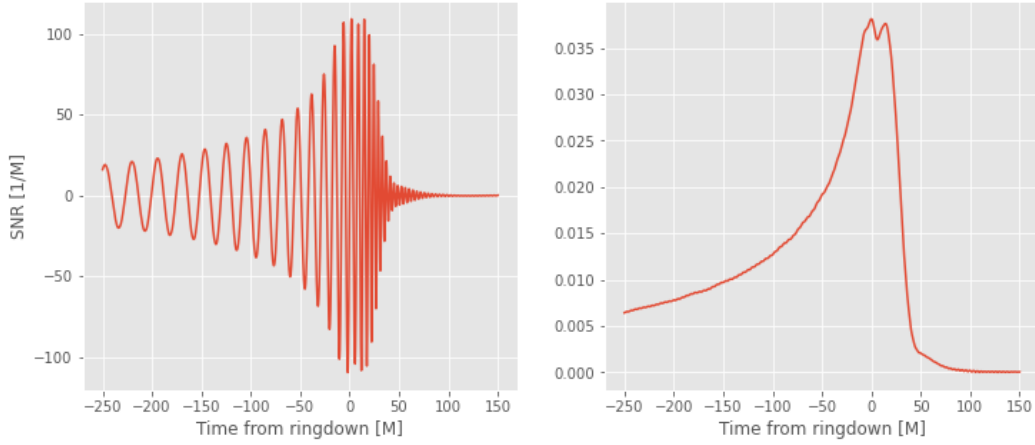


Figure 6.6: Time series for h_+ (left) and amplitude for the ET. Spins $\chi_z^1 = \chi_z^2 = 0.9$, mode (4,4) and $M = 130 M_\odot$.

good impression of how this ratio evolves with changing mass.

The plot with horizon distances, figure 6.9, looks largely similar. The SNRs/distances have increased and the (3,2) mode has also become relatively more important.

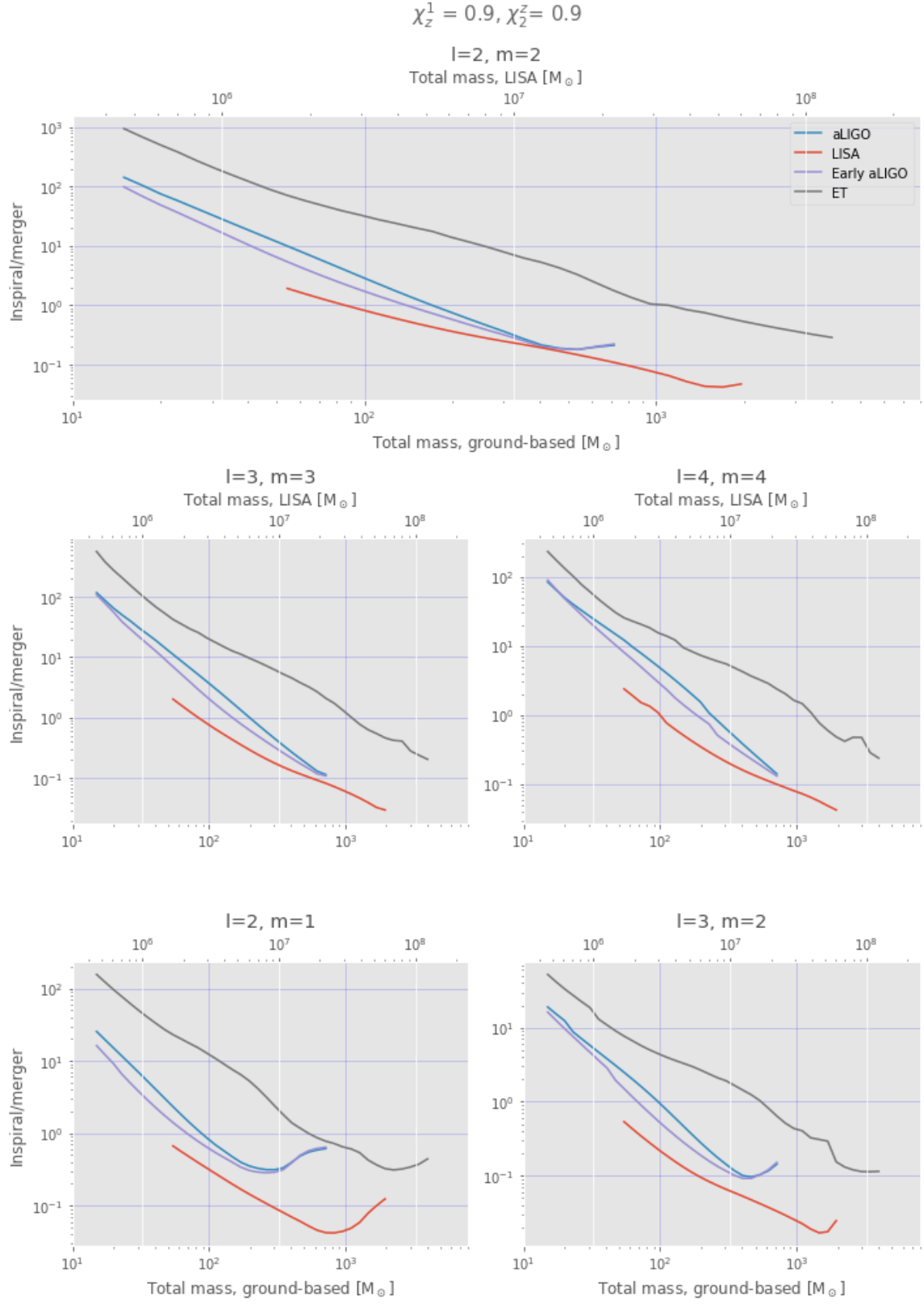


Figure 6.7: SNR ratios of inspiral/merger for large aligned spins.

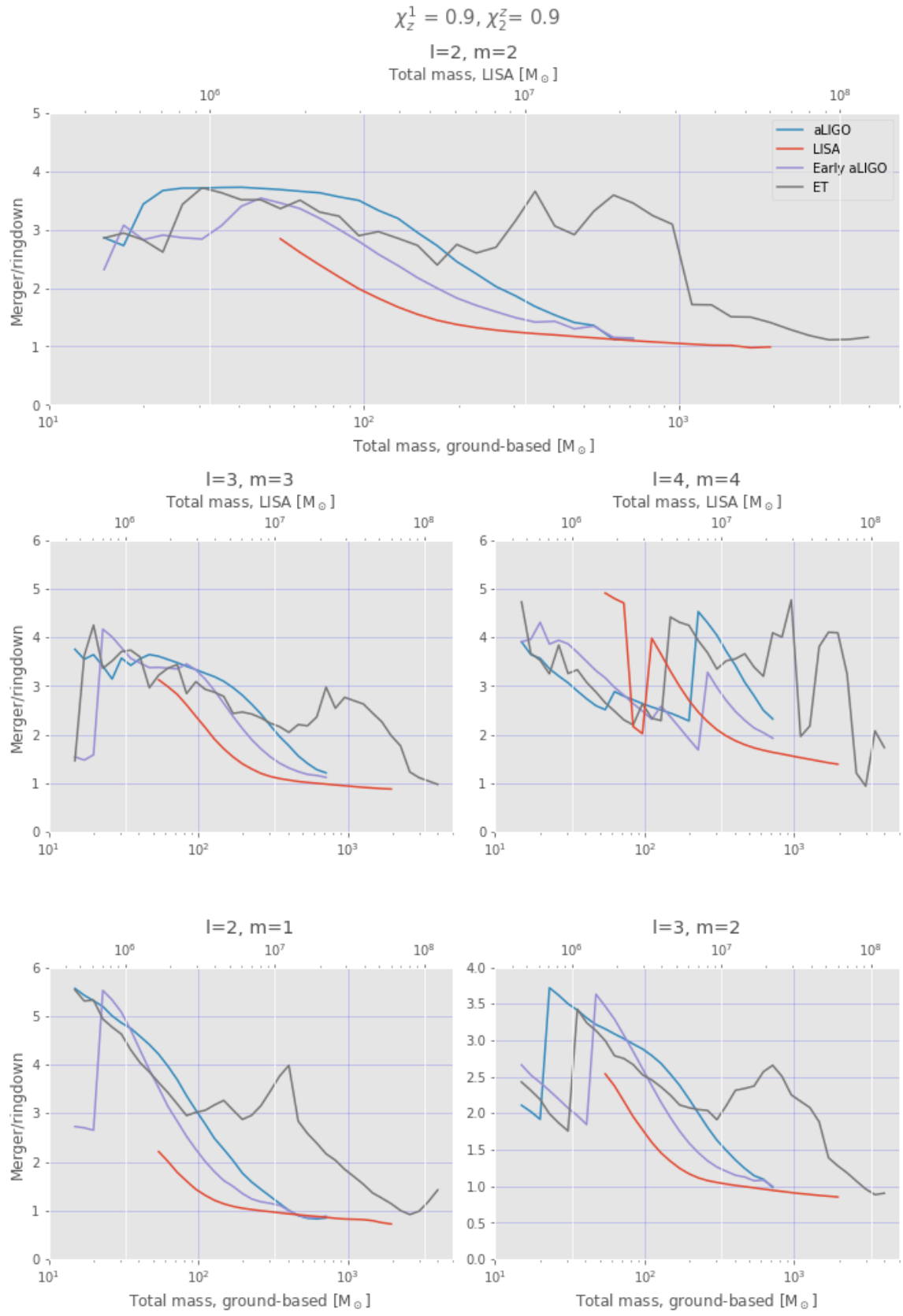


Figure 6.8: SNR ratios of merger/ringdown large aligned spins.

$$\chi_z^1 = 0.9, \chi_z^2 = 0.9$$

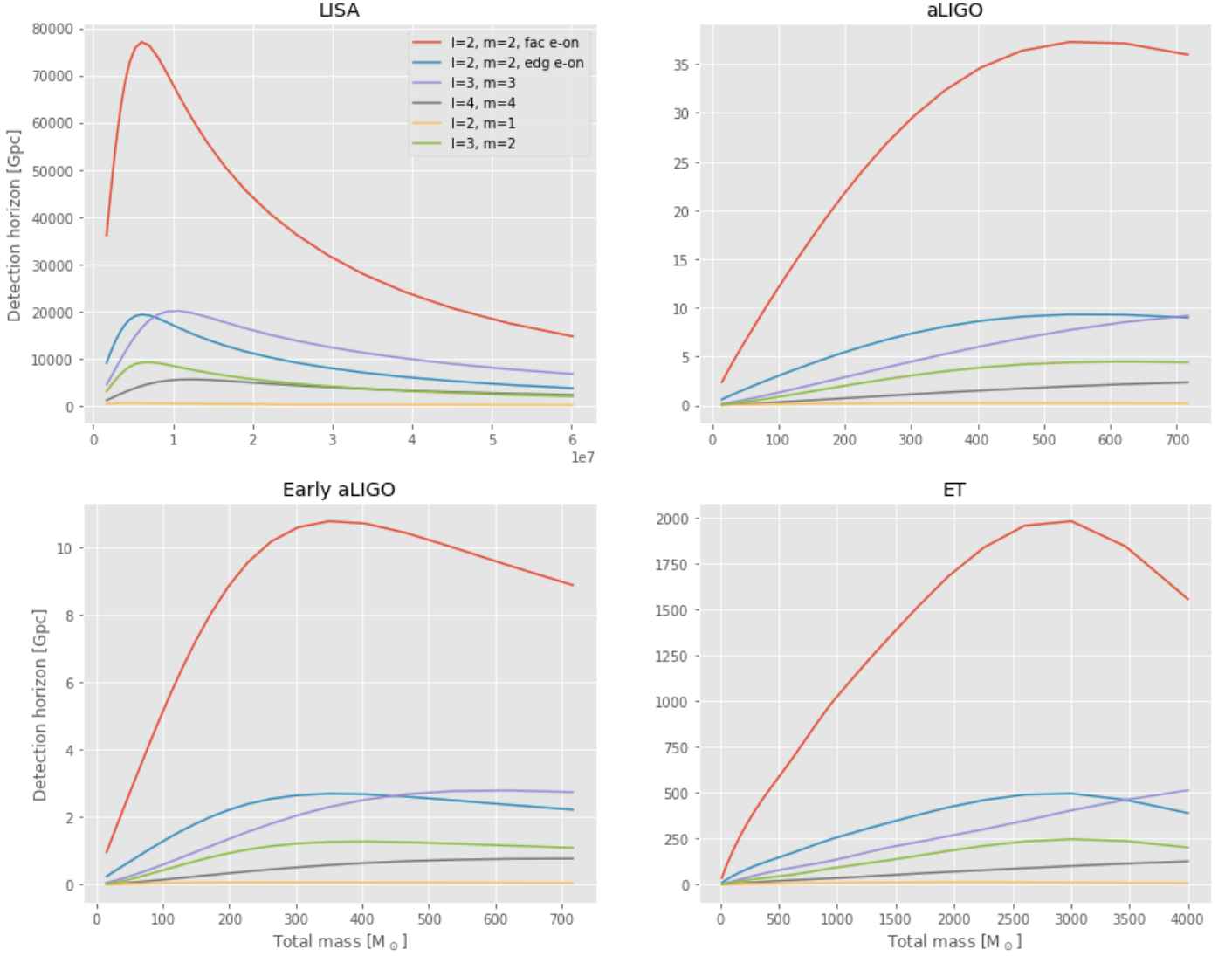


Figure 6.9: Detection horizons for large aligned spins.

Large antiparallel spins

Figures 6.10, 6.11 and 6.12 give the results for large antiparallel spins ($\chi_z^1 = 0.9$ and $\chi_z^2 = -0.9$). Again very little difference can be seen for the inspiral/merger plots. The merger/ringdown ratios also look more or less the same as for the spinless case, but a jump occurs again for the (4,4) modes for the ground-based detectors. For the SNRs and distances the most significant difference is again that the (3,2) mode is a lot more prominent, as was seen for aligned spins.

These ratios don't seem to depend very strongly on the spin. A notable difference is that the merger/ringdown ratios look a lot noisier for the cases with spin. A possible explanation could be that the quality of the waveforms is not at its best for the higher modes at large spin.

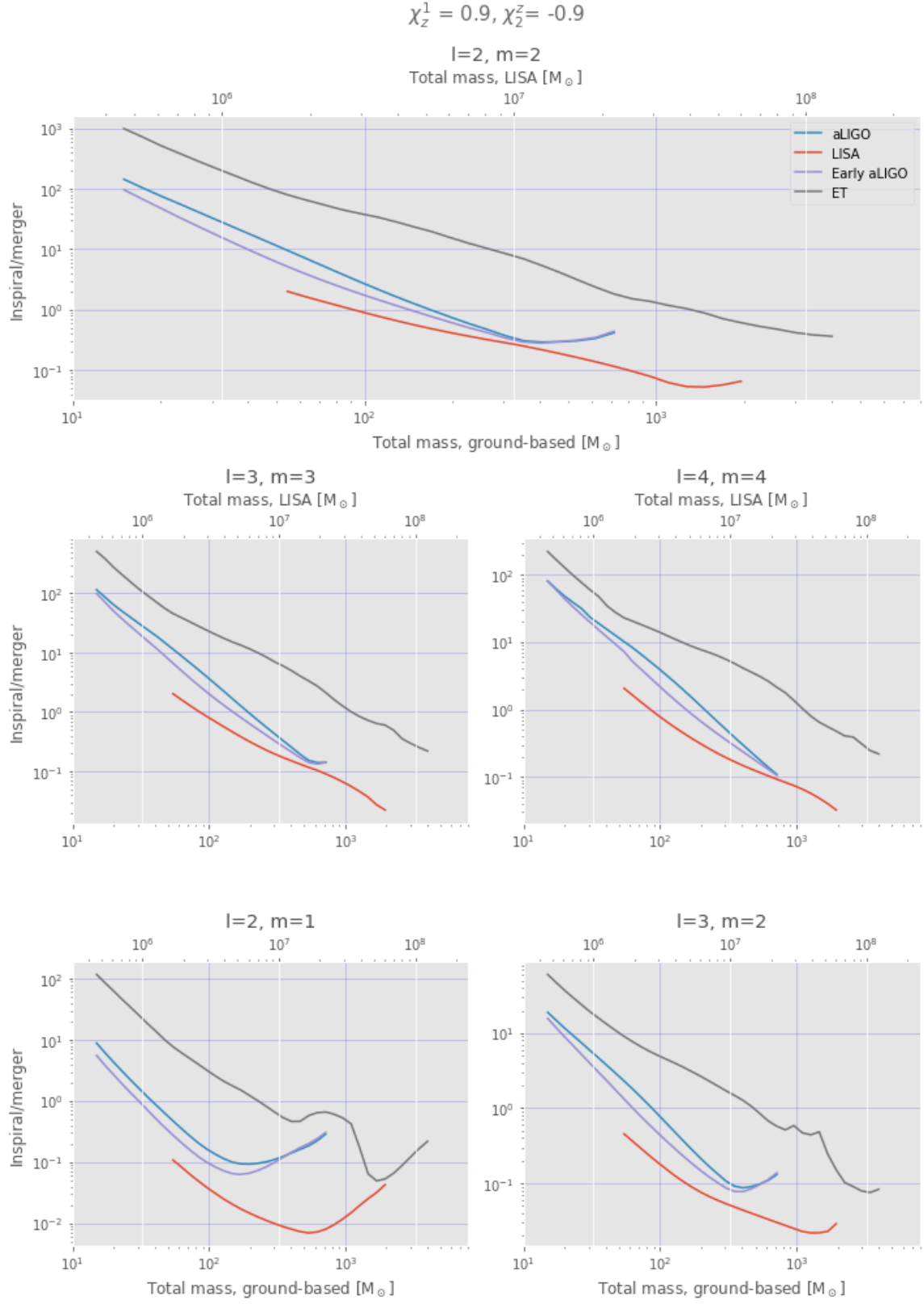


Figure 6.10: SNR ratios of inspiral/merger for large antiparallel spins.

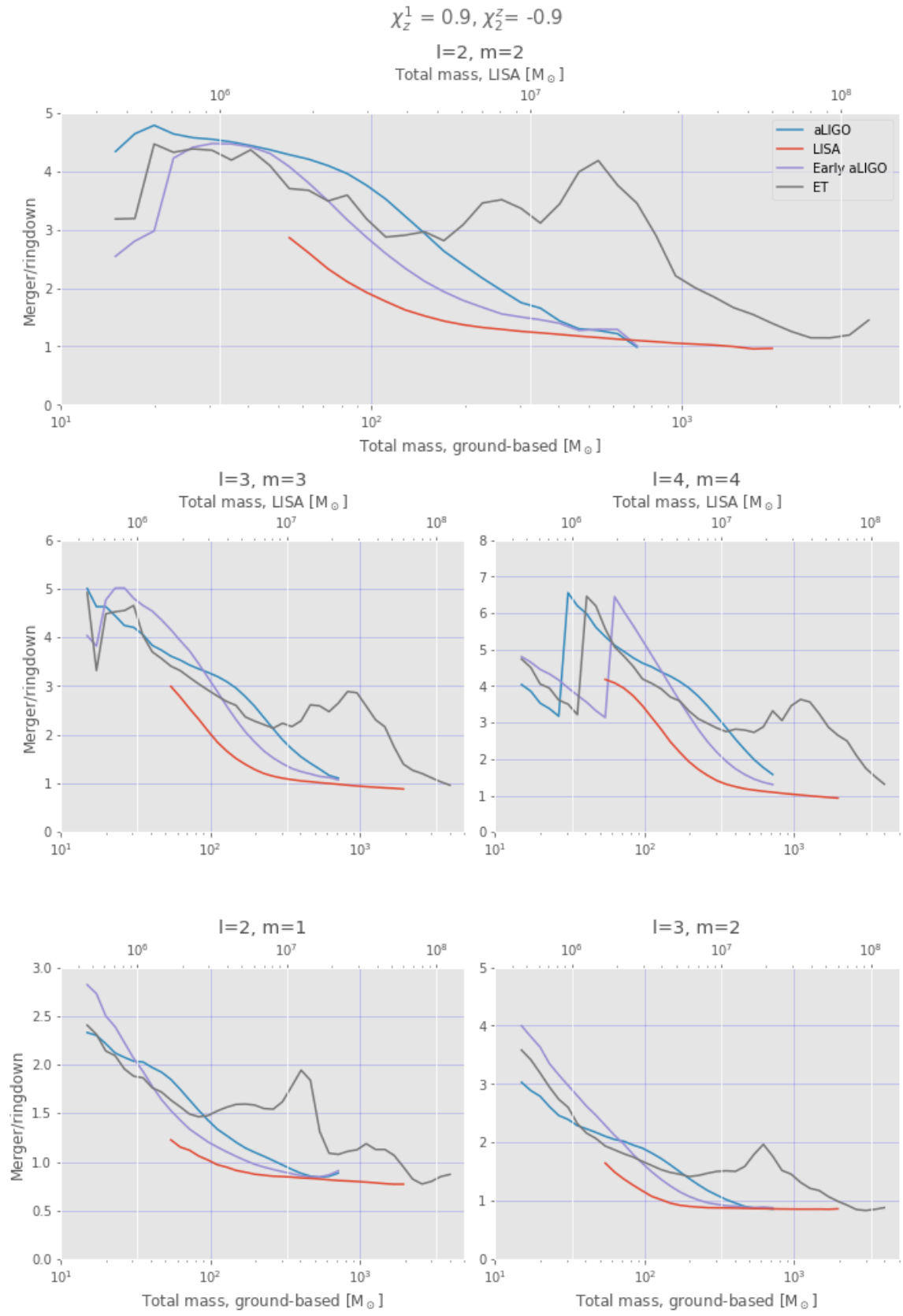


Figure 6.11: SNR ratios of merger/ringdown for large antiparallel spins.

$$\chi_z^1 = 0.9, \chi_z^2 = -0.9$$

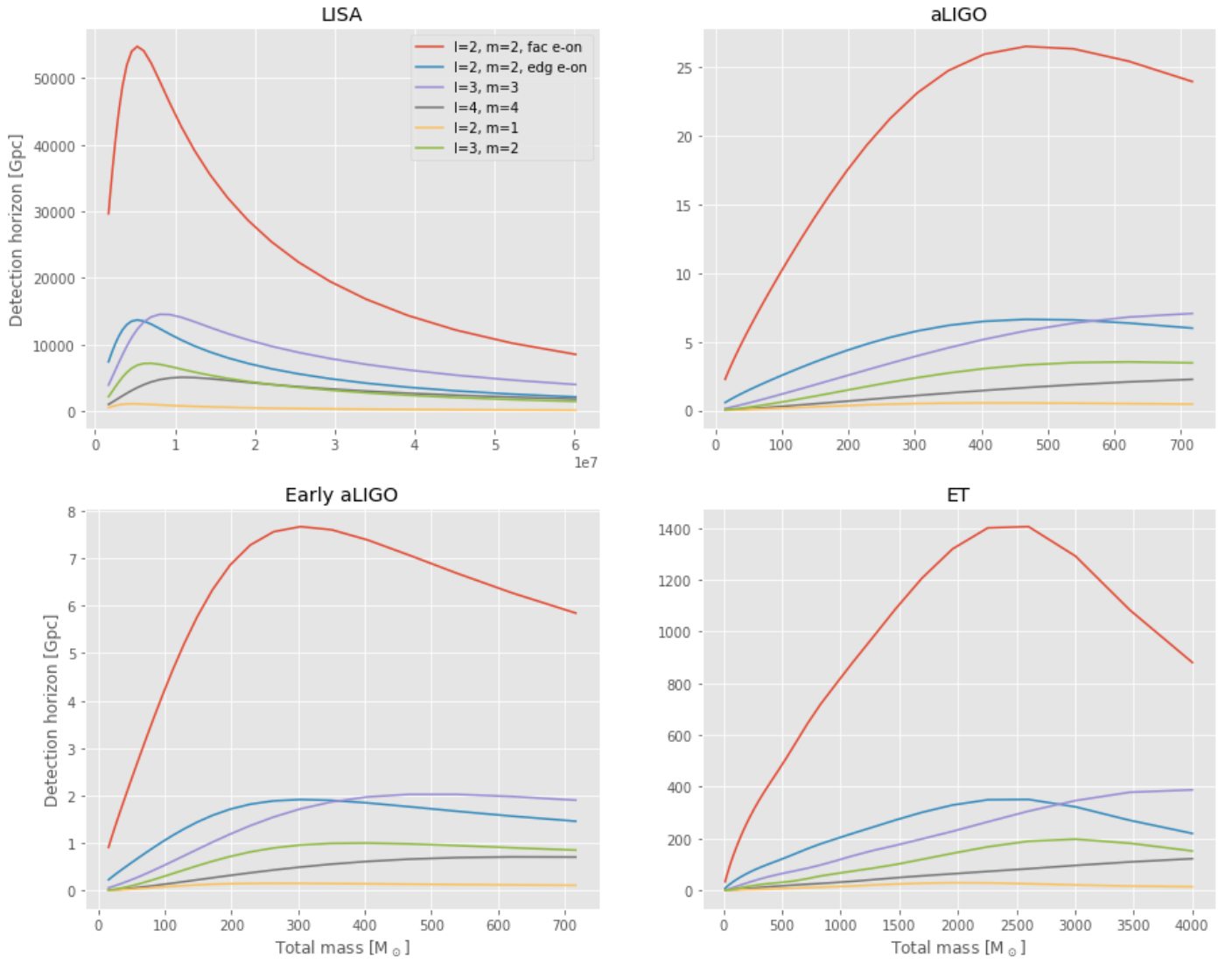


Figure 6.12: Detection horizons for large antiparallel spins.

Model comparison

A comparison is now made of the performance of the waveform models that were described in section 3.4. To see how they perform across the parameter space, one can vary the parameters and how similar the resulting waveforms are, which can be quantified by the overlap (equation 3.13). Instead of the overlap the mismatch \mathcal{M} is used here, which is related to the overlap $\mathcal{O}(\theta)$ for parameters θ as

$$\mathcal{M}(\theta) = 1 - \mathcal{O}(\theta) = 1 - \frac{(h_1(\theta)|h_2(\theta))}{\sqrt{(h_1(\theta)|h_1(\theta))(h_2(\theta)|h_2(\theta))}}, \quad (7.1)$$

where $h_{1,2}(\theta)$ denote the strains of the models that are being compared. This means the mismatch can have a value between 0 and 1, where a value close to 0 signifies good agreement between the waveforms. When the SNR is low enough, a small difference between models doesn't have to be a problem when the difference is small compared to the noise. When increasing the SNR the difference between the waveforms will become significant at some point. The range the models are indistinguishable can be approximated by [61]

$$\mathcal{M} < \frac{D}{\rho^2}, \quad (7.2)$$

where \mathcal{M} is the mismatch, D the number of parameters describing the system and ρ the SNR.

Figure 7.1 shows a grid that demonstrates how the mismatch varies with changing spin for LIGO. These mismatches have been converted to the maximum SNR at which the waveforms are indistinguishable by using equation 7.2. This makes it clear that the mismatch heavily depends on the spin and that the results are very different for different sets of models. Unfortunately this kind of plots cannot be used to comprehensively describe the performance of the different models. A problem is that the parameter space is very large; the mass ratio, total mass, spins and inclination can be varied for each of the modes, for each set of waveform models and for each detector. In order to be able to give a good impression of the model performance across the full parameter space a stochastic exploration is used.

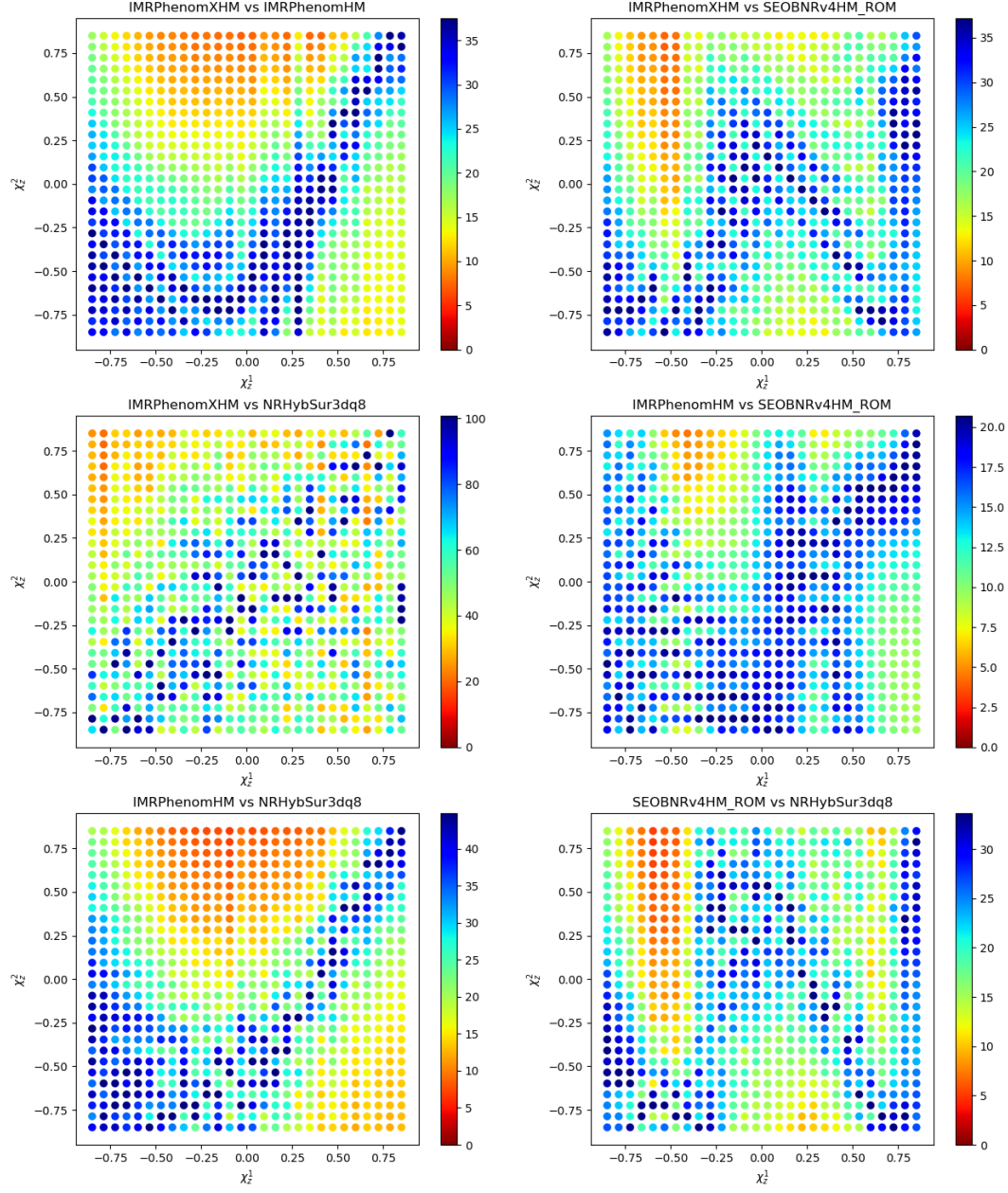


Figure 7.1: Grid of maximum SNR satisfying the indistinguishability criterion (equation 7.2) for varying spins. It shows the (2,2) mode for LIGO, using mass ratio $q = 2$ and total mass $M = 100 M_{\odot}$.

7.1 Monte Carlo simulation

A Monte Carlo simulation is used to explore the parameter space. Random points are sampled from the parameter space and for each of these a mismatch is computed.

In the simulation the mass ratio q is randomly select from a uniform distribution between 1 and 8. The spins are selected from a uniform distribution between -0.8 and 0.8 and finally the orientation is also randomly selected, with every orientation having equal probability. A histogram of the mismatches is made for each combination of the four models and for each of the detectors. For the ground-based detectors this is done separately for three different masses: $15 M_{\odot}$, $80 M_{\odot}$ and $400 M_{\odot}$. For LISA the same scale factor as in the previous chapter is used (3.1×10^4), but the smallest mass is omitted because this falls outside the range of LISA where the approximations apply. This means that the used masses for LISA are $2.5 \times 10^6 M_{\odot}$ and $1.2 \times 10^7 M_{\odot}$. For each of the models all of the available modes are used. A set of 2000 samples was used for each combination of mass, detector and set of models.

7.2 Results

A histogram was made for the logarithm of the mismatches and these are shown in figures 7.2, 7.3 and 7.4. It can be seen that the mismatches cover a large range of magnitudes, with the logarithms varying from -0.5 to about -5.

The histograms in figure 7.2 compare IMRPhenomXHM and IMRPhenomHM to NRHybSur3dq8. It shows that the matches typically become better with decreasing mass. The differences between the ET and LIGO are quite small. For LISA the smaller mass looks more or less similar to the others, but for the larger mass the mismatches are not quite as good. The results for IMRPhenomXHM are clearly better than those for IMRPhenomHM, as was to be expected.

Figure 7.3 again shows mismatches for IMRPhenomXHM and IMRPhenomHM, this time against SEOBNRv4HM_ROM. It can be seen again that the matches become a bit worse as the mass increases, though not as clearly as in figure 7.2. The results for LISA are again similar for the medium mass, but clearly worse for the largest mass. Overall the results for NRHybSur3dq8 were a bit better, though one also has to consider that the frequency range is a bit shorter for NRHybSur3dq8.

Finally the phenomenological models are compared to each other in figure 7.4, which also shows mismatches between SEOBNRv4HM_ROM and NRHybSur3dq8. For the phenomenological models we can see again that the matches get better as the mass decreases. The ET and LIGO look largely similar, except for the results for the small mass, which has a wider distribution for the ET. LISA results are worse again, mostly for the large mass.

Comparing NRHybSur3dq8 to SEOBNRv4HM_ROM shows smaller dependence on the mass for the ET and LIGO. For LISA we see again that the performance is not as good for the large mass, but this time the medium mass actually shows better matches.

Overall the best matches were seen between IMRPhenomXHM and NRHybSur3dq8,

but as mentioned before there are more things to consider, such as the smaller length of NRHybSur3dq8. It can be confirmed that IMRPhenomXHM gives better results than its predecessor IMRPhenomHM. In many cases the matches are better for the lower masses, where the inspiral is more pronounced, as concluded in chapter 6. The ET and LIGO showed largely similar behaviour, whereas the performance for LISA was generally not as good. The large mass for LISA showed the worst results overall. It needs to be repeated that this does depend on the choice for the scaling factor for LISA. When using the full LISA response the range can be extended to lower masses and the other results suggest that this might lead to better matches for LISA.

Since LISA will have SNRs of up to a few 1000 the current waveform models will lead to significant systematic errors in parameter estimation. Even an SNR of 100 will already require a mismatch of roughly 10^{-4} (only very few mismatches were found to be this small) to avoid systematic errors according to the approximation of equation 7.2. The same conclusion can be drawn with regard to the ET, for which the SNR can also be over 100 [25].

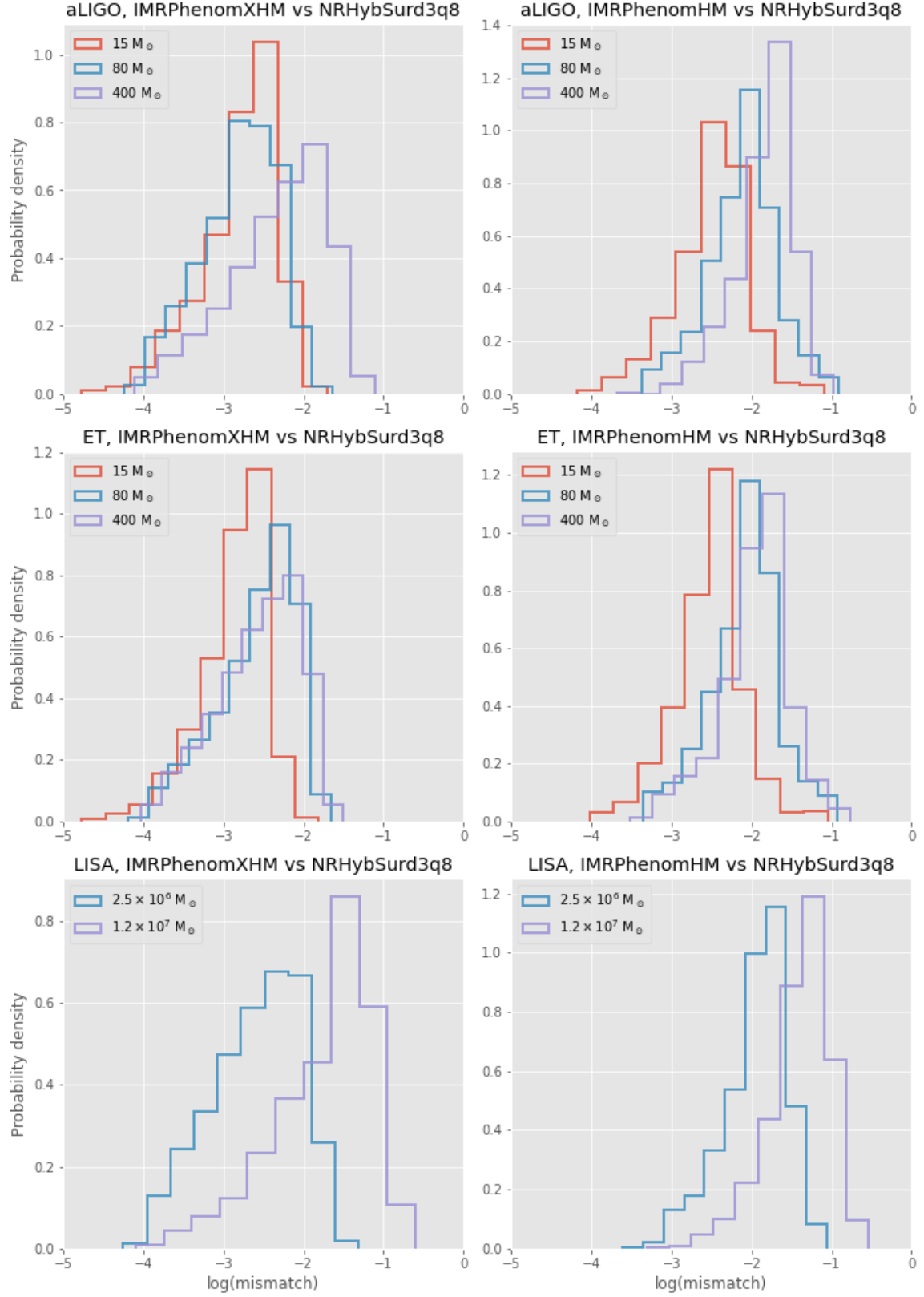


Figure 7.2: Mismatches for IMRPhenomXHM and IMRPhenomHM against NRHybSurd3q8.

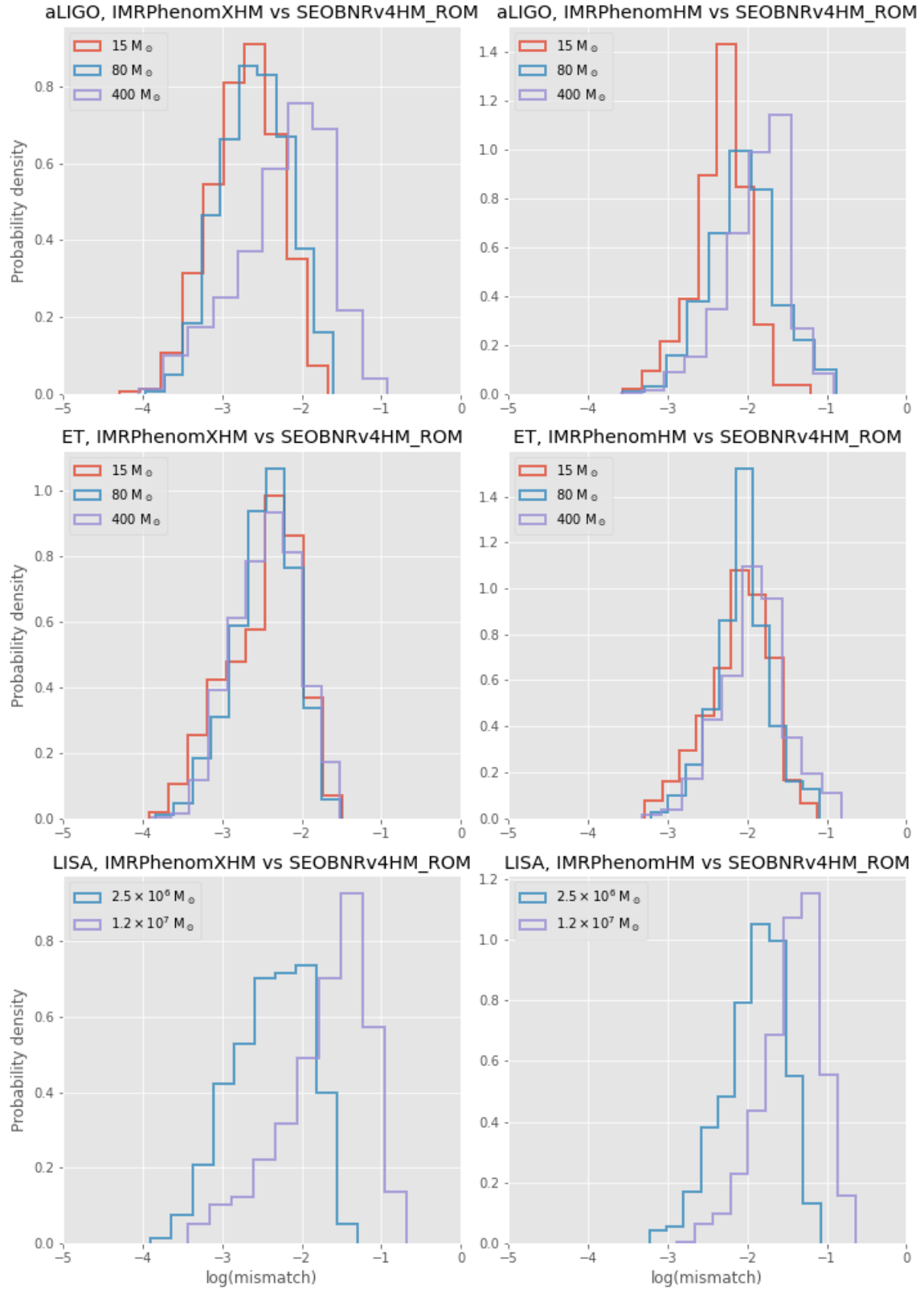


Figure 7.3: Mismatches for IMRPhenomXHM and IMRPhenomHM against SEOBNRv4HM_ROM.

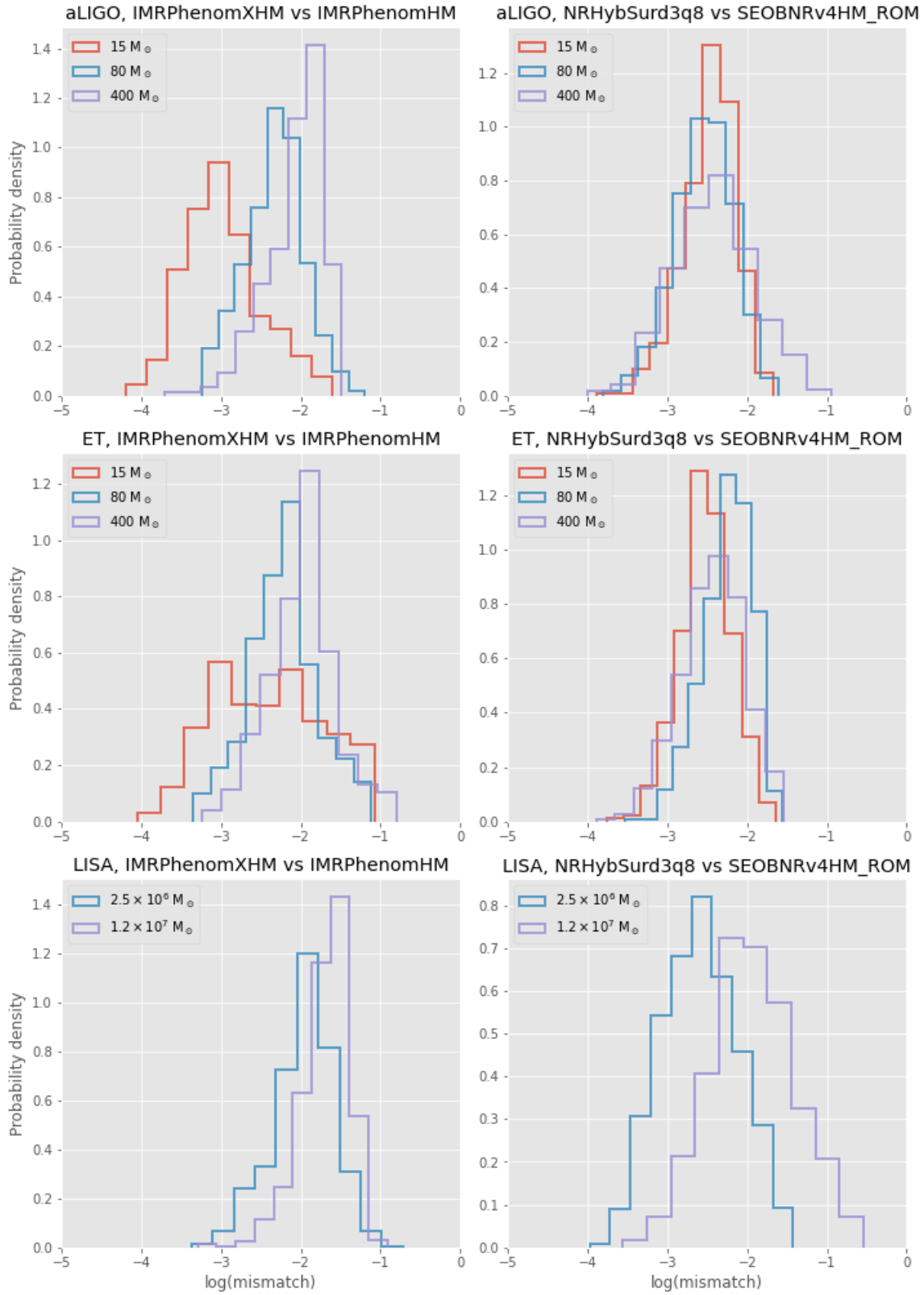


Figure 7.4: Mismatches for IMRPhenomXHM vs IMRPhenomHM and SEOBNRv4HM_ROM vs NRHyb-Sur3dq8.

Conclusions

In this work an analysis and comparison was made of the characteristics of the LIGO, Einstein Telescope and LISA gravitational wave detectors. Doing this can help us to understand how data analysis will be different for the future LISA and ET detectors, when compared to the LIGO-type detectors that are currently used. The differences in their sensitivity curves cause them to have different responses to the same (or properly scaled) source. This also influences the performance of waveform models.

It was found that the ET puts more emphasis on the inspiral, whereas the merger is more pronounced for LISA. The relative importance of the merger and ringdown are more on the same scale for each of the detectors. All of this does not strongly depend on the spins. The fact that the detectors emphasize different parts of the waveform means that the performance of waveform models may also be different.

The three most important families of waveform models that are used in parameter estimation were compared to each other for each of the detectors. The used models were the phenomenological models IMRPhenomXHM [53] and IMRPhenomHM [52], the effective one-body reduced order model SEOBNRv4HM_ROM [54] and the hybrid surrogate model NRHybSur3dq8 [55]. All of these models contain higher modes and are non-precessing. The best matches were found between IMRPhenomXHM and NRHybSur3dq8. The performance for LIGO and the ET were roughly similar, whereas the results for LISA were, mostly for the larger mass, not as good. This is influenced by the choice for the scaling factor between ground-based detectors and LISA and these results could be better when extending the LISA range to lower masses. Current values for the mismatches between the waveform models would mean that systematic errors would occur in parameter estimation for LISA and the ET. This means that, with the current models, they won't be able to make optimal use of their very high SNR values.

For further research it would be interesting in the first place to use the full LISA response so that the considered range can be extended to lower masses, which perhaps

will lead to better results for the matches. Furthermore it could be interesting to try to find out more about the processes underlying the mismatch distributions. One could, for example, try to find out how it is influenced by spin and mass ratio, or split the mismatches into parts caused by the inspiral, merger and ringdown. Similar analyses can be made for precessing waveform models.

In summary the future LISA and Einstein Telescope gravitational wave detectors will bring up many new challenges in data analysis, but surely the results will be very exciting.

Bibliography

- [1] Abbott et al., *Observation of Gravitational Waves from a Binary Black Hole Merger*, Phys. Rev. Lett. 116, 061102, 2016
- [2] Amaro-Seoane et al., *Laser Interferometer Space Antenna*, the accepted LISA L3 proposal, 2017
- [3] <https://lisa.nasa.gov/>, LISA website of NASA, viewed 7-8-2020
- [4] Marsat et al., *Exploring the Bayesian parameter estimation of binary black holes with LISA*, arXiv:2003.00357, 2020
- [5] Harms and Paik, *Newtonian-noise cancellation in full-tensor gravitational-wave detectors*, Phys. Rev. D 92, 022001, 2015
- [6] Harms et al., *Low-Frequency Terrestrial Gravitational-Wave Detectors*, Phys. Rev. D 88, 122003, 2013
- [7] Luo et al., *A brief analysis to Taiji: Science and technology*, Elsevier, 2019
- [8] Kawamura et al., *Current status of space gravitational wave antenna DECIGO and B-DECIGO*, arXiv:2006.13545, 2020
- [9] Luo et al., *TianQin: A space-borne gravitational wave detector*, Class. Quant. Grav. 33(3), 2015
- [10] Armano et al., *The LISA Pathfinder Mission*, Journal of Physics: Conference Series 610 012005, 2015
- [11] Armano et al., *Beyond the Required LISA Free-Fall Performance: New LISA Pathfinder Results down to 20 μ Hz*, Phys. Rev. Lett. 120, 061101, 2018
- [12] Armano et al., *Sub-Femto-g Free Fall for Space-Based Gravitational Wave Observatories: LISA Pathfinder Results*, Phys. Rev. Lett. 116, 231101, 2016
- [13] Kupfer et al., *LISA verification binaries with updated distances from Gaia Data Release 2*, arXiv:1805.00482, 2018
- [14] Volonteri, *Formation of Supermassive Black Holes*, The Astronomy and Astrophysics Review, vol. 18, pp. 279–315, arXiv:1003.4404, 2010

- [15] Chillingran et al., *A Population of Bona Fide Intermediate-mass Black Holes Identified as Low-luminosity Active Galactic Nuclei*, Astrophys. J. 863(1):1, 2018
- [16] Amaro Seoanne et al., *Intermediate and Extreme Mass-Ratio Inspirals – Astrophysics, Science Applications and Detection using LISA*, Class. Quant. Grav. 24:R113-R169, 2007
- [17] Sesana, *The promise of multi-band gravitational wave astronomy after GW150914*, Phys. Rev. Lett. 116, 231102, 2016
- [18] Del Pozzo, *Measuring the Hubble constant using gravitational waves*, Journal of Physics: Conference Series 484 012030, 2014
- [19] Abbott et al., *GW170817: Observation of Gravitational Waves from a Binary Neutron Star Inspiral*, Phys. Rev. Lett. 119, 161101, 2017
- [20] Sousa et al., *Full analytical approximation to the stochastic gravitational wave background*, Phys. Rev. D 101, 103508, 2020
- [21] Armstrong et al., *Time-Delay Interferometry for Space-based Gravitational Wave Searches*, Astrophys. J. 527-22, 1999
- [22] Prince et al., *The LISA Optimal Sensitivity*, Phys. Rev. D 66 122002, 2002
- [23] Miquel Trias, *Gravitational wave observation of compact binaries*, PhD thesis UIB, 2010
- [24] Adhikari, *Gravitational Radiation Detection with Laser Interferometry*, Rev. Mod. Phys. 86. 121, 2014
- [25] Maggiore et al., *Science Case for the Einstein Telescope*, arXiv:1912.02622, 2020
- [26] Sathyaprakash et al., *Cosmology and the Early Universe*, arXiv:1903.09260, 2019
- [27] www.ligo.caltech.edu, LIGO website of Caltech
- [28] <https://www.ligo.org/>, LIGO website
- [29] Hild et al., *Sensitivity Studies for Third-Generation Gravitational Wave Observatories*, Class. Quant. Grav. 28 (9), 2010
- [30] Hild et al., *Pushing towards the ET sensitivity using 'conventional' technology*, arXiv:0810.0604, 2008
- [31] Hild et al., *A Xylophone Configuration for a third Generation Gravitational Wave Detector*, Class. Quant. Grav. 27:015003, 2010
- [32] Thrane and Talbot, *An introduction to Bayesian inference in gravitational-wave astronomy: parameter estimation, model selection, and hierarchical models*, Publications of the Astronomical Society of Australia 37 E036, 2018
- [33] Abbott et al., *Properties of the Binary Black Hole Merger GW150914*, Phys. Rev. Lett. 116, 241102, 2016
- [34] <https://www.astro.umd.edu/~miller/teaching/astr498/lecture24.pdf>, lecture material from C. Miller, University of Maryland

- [35] Mapelli, *Binary Black Hole Mergers: Formation and Populations*, Front. Astron. Space Sci., 2020
- [36] Gratton et al., *What is a Globular Cluster? An observational perspective*, The Astronomy and Astrophysics Review, 27:8, 2019
- [37] Neumayer et al., *Nuclear Star Clusters*, The Astronomy and Astrophysics Review, 28:4, 2020
- [38] Portegies Zwart et al., *Young massive star clusters*, Annu. Rev. Astron. Astrophys. 48, 431–493, 2010
- [39] C.J. Lada and E.A. Lada, *Embedded Clusters in Molecular Clouds*, Ann. Rev. Astron. Astrophys. 41:57-115, 2003
- [40] Hills and Fullerton, *Computer simulations of close encounters between single stars and hard binaries*, Astrophys. J. 85, 1281–1291, 1980
- [41] Ziosi et al., *Dynamics of stellar black holes in young star clusters with different metallicities - II. Black hole-black hole binaries*, Mnthly. Notices R Astron. Soc. 441, 3703–3717, 2014
- [42] Rodriguez et al., *Illuminating black hole binary formation channels with spins in advanced LIGO*, Astrophys. J. Lett. 832:L2, 2016
- [43] Rodriguez et al., *A Compact Supermassive Binary Black Hole System*, Astrophys. J. 646 Issue 1, 49-60, 2006
- [44] Deane et al., *A close-pair binary in a distant triple supermassive black hole system*, Nature volume 511, pp. 57–60, 2014
- [45] Milosavljević and Merritt, *The Final Parsec Problem*, AIP Conf. Proc. 686-1, 201-210, 2003
- [46] Ryu et al., *Interactions between multiple supermassive black holes in galactic nuclei: a solution to the final parsec problem*, MNRAS 473, pp. 3410–3433, 2018
- [47] Ryu et al., *Collisionless loss-cone refilling: there is no final parsec problem*, MNRAS 464-2, pp. 2301–2310, 2017
- [48] Cecilio García Quirós *Waveform modelling of binary black holes in the advanced LIGO era*, PhD thesis UIB, 2020
- [49] Metropolis et al., *Equation of State Calculations by Fast Computing Machines*, The Journal of Chemical Physics, 21, 1087, 1953
- [50] Hastings, *Monte Carlo sampling methods using Markov chains and their applications*, Biometrika, Volume 57, Issue 1, Pages 97–109, 1970
- [51] Buonanno and Damour, *Effective one-body approach to general relativistic two-body dynamics*, Phys. Rev. D 59, 084006, 1999
- [52] London et al., *First higher-multipole model of gravitational waves from spinning and coalescing black-hole binaries*, Phys. Rev. Lett. 120, 161102, 2018

- [53] García-Quirós et al., *IMRPhenomXHM: A multi-mode frequency-domain model for the gravitational wave signal from non-precessing black-hole binaries*, Phys. Rev. D 102, 064002, 2020
- [54] Cotesta et al., *Frequency-domain reduced-order model of aligned-spin effective-one-body waveforms with higher-order modes*, Phys. Rev. D 101, 124040, 2020
- [55] Varma et al., *Surrogate model of hybridized numerical relativity binary black hole waveforms*, Phys. Rev. D 99, 064045, 2019
- [56] Pratten et al., *Setting the cornerstone for the IMRPhenomX family of models for gravitational waves from compact binaries: The dominant harmonic for non-precessing quasi-circular black holes.*, Phys. Rev. D 102, 064001, 2020
- [57] Pratten et al., *Let's twist again: computationally efficient models for the dominant and sub-dominant harmonic modes of precessing binary black holes*, arXiv:2004.06503, 2020
- [58] Wahlquist, Estabrook, *Response of Doppler spacecraft tracking to gravitational radiation*, General Relativity and Gravitation, Volume 6, Issue 5, pp.439-447, 1975
- [59] Marsat and Baker, *Fourier-domain modulations and delays of gravitational-wave signals*, arXiv:1806.10734v1, 2018
- [60] Joseph Weber, *Evidence for discovery of gravitational radiation*, Phys. Rev. Lett., 22, 1320, 1969
- [61] Boyle et al., *The SXS Collaboration catalog of binary black hole simulations*, Class. Quant. Grav. 36, 195006, 2019
- [62] Abbott et al., *GW190521: A Binary Black Hole Merger with a Total Mass of 150 M_{\odot}* , Phys. Rev. Lett. 125, 101102, 2020